Memo version 1.0

# BESIII Analysis Memo

**DocDB-XXX**

**BAM-XXX**

**August 10, 2019**

# Amplitude Analysis and Branching Fraction Measurement of $D_s^+ \to K^+K^-\pi^+$

Meng Wang[a], Yu Lu[a], and Liaoyuan Dong[a], and Huaimin Liu[a]

[a]*Institute of High Energy Physics, CAS*

# Internal Referee Committee

Ref1 xx (Chair)[d], Ref2 xx[e], and Ref3 xx[f]

[d]*Department of Computer Science and Engineering*
[e]*Department of Electrical Engineering*
[f]*Latex Univeristy*

DocDB : http://docbes3.ihep.ac.cn/cgi-bin/DocDB/ShowDocument?docid=XXX

Hypernews : http://hnbes3.ihep.ac.cn/HyperNews/get/paperXXX.html

## Abstract

We perform an amplitude analysis of $D_s^+ \to K^+K^-\pi^+$ using a data sample of $3.19 fb^{-1}$ recorded with BESIII detector at a center-of-mass energy of 4.178GeV. About 4000 events are used in amplitude analysis. Amplitudes and phases contributing to this final state are measured. And we also measure the branching fraction of $D_s^+ \to K^+K^-\pi^+$ to be $\mathcal{B}(D_s^+ \to K^+K^-\pi^+) = (5.47 \pm 0.07_{stat.} \pm 0.13_{sys.})\%$.

# Contents

# 1 Introduction

The decay $D_s^+ \to K^+K^-\pi^+$ is Cabibbo-favored (CF) channel and has a large branching fraction and low background contamination. Thus this decay is usually suited as a reference channel for other decays of the $D_s$ meson and used to normalize measurements of decay chains involving charm quarks. An accurate knowledge of its substructure is important to reduce systematic uncertainties in analyses that use this channel. Study of a given state can also illuminates light meson spectroscopy and shed light on different production mechanisms.

## 1.1 The scalar meson $f_0(980)$ and $a_0(980)$

The Constituent Quark Model has been very successful in the past few decades by explaining how hadrons are made up. Base on this model, the nonets of pseudo-scalar, vector and tensor mesons are now well identified. However, the identification of the scalar mesons is still uncertain due to the broad widths and the lack of a distinctive angular distribution. Among the candidates for the spin-parity $J^{PC} = 0^{++}$ nonet, the parameters of some states such as $f_0(980)$ and $a_0(980)$ are not well measured. For $f_0(980)$, as it is very close to $K\bar{K}$ threshold and has strong coupling to $\pi\pi$ and $K\bar{K}$ final states, its parameters are still uncertain.

According to the amplitude analysis of $D_s^+ \to \pi^+\pi^0\eta$ [1], the decay $D_s^+ \to a_0(980)^0\pi^+$ is observed. However, $f_0(980)$ and $a_0(980)$ are very close to each other and it is very difficult to distinguish them.

From the Dalitz plot analysis of $D_s^+ \to \pi^+\pi^-\pi^+$, we can get the branching fraction $\mathcal{B}(D_s^+ \to f_0(980)\pi^+, f_0(980) \to \pi^+\pi^-)$. Then if we know the branching ratio of $\Gamma_{f_0(980)}(K^+K^-)/\Gamma_{f_0(980)}(\pi^+\pi^-)$, we can obtain:

$$\mathcal{B}(D_s^+ \to f_0(980)\pi^+, f_0(980) \to K^+K^-) = \mathcal{B}(D_s^+ \to f_0(980)\pi^+, f_0(980) \to \pi^+\pi^-)\frac{\Gamma_{f_0(980)}(K^+K^-)}{\Gamma_{f_0(980)}(\pi^+\pi^-)}. \quad (1)$$

In a similar way, we can obtain:

$$\mathcal{B}(D_s^+ \to a_0(980)\pi^+, a_0(980) \to K^+K^-) = \mathcal{B}(D_s^+ \to a_0(980)\pi^+, a_0(980) \to \pi^0\eta)\frac{\Gamma_{a_0(980)}(K^+K^-)}{\Gamma_{a_0(980)}(\pi^0\eta)}. \quad (2)$$

Then, the ratio of fit fractions of $D_s^+ \to f_0(980)\pi^+$ and $D_s^+ \to a_0(980)\pi^+$ $\Gamma$ is:

$$\Gamma = \frac{\mathcal{B}(D_s^+ \to f_0(980)\pi^+, f_0(980) \to \pi^+\pi^-)\frac{\Gamma_{f_0(980)}(K^+K^-)}{\Gamma_{f_0(980)}(\pi^+\pi^-)}}{\mathcal{B}(D_s^+ \to a_0(980)\pi^+, a_0(980) \to \pi^0\eta)\frac{\Gamma_{a_0(980)}(K^+K^-)}{\Gamma_{a_0(980)}(\pi^0\eta)}}. \quad (3)$$

If we can get the value of $\Gamma$ in Eq. 3, it's possible to fix the ratio in amplitude analysis and then distinguish $f_0(980)$ and $a_0(980)$ at the low end of $K^+K^-$ mass spectrum. Using isospin relations, the

relation between $\Gamma_{f_0(980)}(\pi\pi)/\Gamma_{f_0(980)}(\pi\pi + K\bar{K})$ and $\Gamma_{f_0(980)}(K^+K^-)/\Gamma_{f_0(980)}(\pi^+\pi^-)$ is:

$$\frac{\Gamma_{f_0(980)}(K^+K^-)}{\Gamma_{f_0(980)}(\pi^+\pi^-)} = \frac{3}{4}\cdot\left[\frac{1}{\frac{\Gamma_{f_0(980)}(\pi\pi)}{\Gamma_{f_0(980)}(\pi\pi)+\Gamma_{f_0(980)}(K\bar{K})}} - 1\right]. \tag{4}$$

However the value of $\Gamma_{f_0(980)}(K^+K^-)/\Gamma_{f_0(980)}(\pi^+\pi^-)$ is not well measured as is shown in Table 1 [2]. So we have to extract the $\mathcal{S}$ wave line shape at the low end of $K^+K^-$ mass spectrum in a quasi-model-independent way. In other words, we take $a_0(980)$ and $f_0(980)$ as a whole in amplitude analysis.

Table 1: The $f_0(980)$ branching ratio $\Gamma_{f_0(980)}(\pi\pi)/\left[\Gamma_{f_0(980)}(\pi\pi) + \Gamma_{f_0(980)}(K\bar{K})\right]$

| value | Collaboration | comment |
|---|---|---|
| $0.52 \pm 0.12$ | BABAR | $B^{\pm} \to K^{\pm}\pi^{\pm}\pi^{\mp}$ [3] |
| $0.75^{+0.11}_{-0.13}$ | BESII | $\chi_{c0} \to 2\pi^+2\pi^-, \pi^+\pi^-K^+K^-$ [4] |
| $0.84 \pm 0.02$ | SPEC | Combined fit [5] |

## 1.2 The $D_s^+ \to K^+K^-\pi^+$ decay

Hadronic decays of mesons with charm are an important tool for understanding the dynamics of the strong interaction in the low energy regime. Fig. 1 illustrates main Feynman diagrams related to the decay. The main contribution comes from the tree diagram with an internal $W^+$ emission(Fig. 1(a)), that

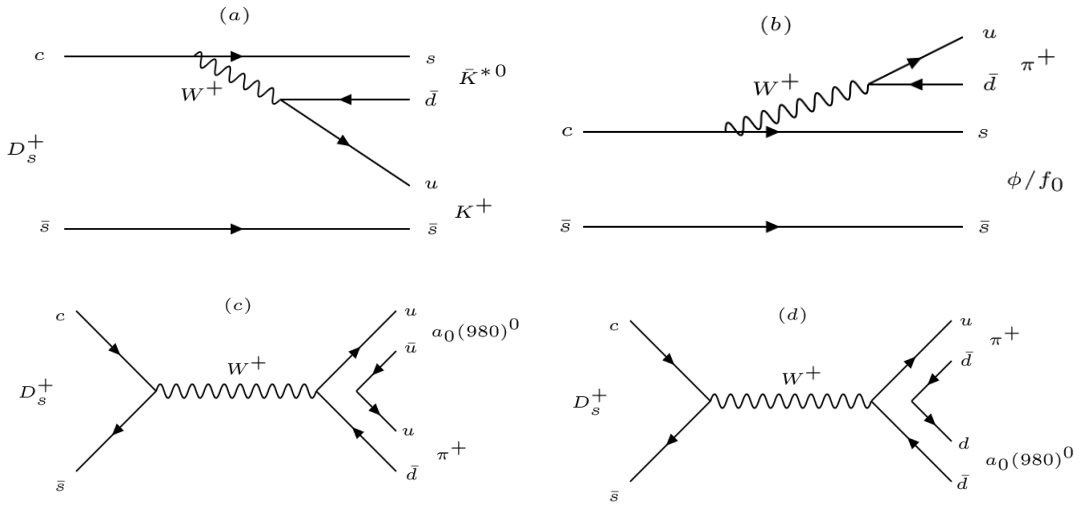


Figure 1: Main Feynman tree diagrams associated with $D_s^+ \to K^+K^-\pi^+$ decay.

describes the $D_s^+ \to \bar{K}^*(892)^0K^+$ decay, and the diagram with an external $W^+$ emission(Fig. 1(b)), that describes the diagram $D_s^+ \to \phi\pi^+/f_0\pi^+$, and the diagram with W-annihilation(Fig. 1(c) and Fig. 1(d)),

that describes the decay $D_s \to a_0(980)^0\pi^+$. Experimental measurements can help to refine theoretical models [6] [7] [8].

### 1.3 Amplitude analysis

Knowledge of the decay amplitude allows us to properly account for interference effects when measuring absolute hadronic branching fractions of $D_s$ mesons. Dalitz plot analyses of this decay mode have been performed by the E687, CLEO and Babar collaborations using 700 events [9], 14400 events [10]a and 96307 events [11], respectively. Table 2 shows the comparision of the fitted decay fractions with the Dalitz plot analyses of previous analyses.

Table 2: previous analyses of this decay channel.

| Decay mode | Fit fraction(BABAR) | Fit fraction(CLEO-c) | Fit fraction(E687) |
|---|---|---|---|
| $D_s^+ \to \bar{K}^*(892)^0K^+$ | 47.9±0.5±0.5 | 47.4±1.5±0.4 | 47.8±4.6±4.0 |
| $D_s^+ \to \phi(1020)\pi^+$ | 41.4±0.8±0.5 | 42.2±1.6±0.3 | 39.6±3.3±4.7 |
| $D_s^+ \to f_0(980)\pi^+/a_0(980)\pi^+$ | 16.4±0.7±2.0 | 28.2±1.9±1.8 | 11.0±3.5±2.6 |
| $D_s^+ \to \bar{K}_0^*(1430)^0K^+$ | 2.4±0.3±1.0 | 3.9±0.5±0.5 | 9.3±3.2±3.2 |
| $D_s^+ \to f_0(1710)\pi^+$ | 1.1±0.1±0.1 | 3.4±0.5±0.3 | 3.4±2.3±3.5 |
| $D_s^+ \to f_0(1370)\pi^+$ | 1.1±0.1±0.2 | 4.3±0.6±0.5 | ... |
| $\sum FF(\%)$ | 110.2±0.6±2.0 | 129.5±4.4±2.0 | 111.1 |
| $\chi^2/NDF$ | $\frac{2843}{2305-14} = 1.2$ | $\frac{178}{117} = 1.5$ | $\frac{50.2}{33} = 1.5$ |
| Events | 96307 ± 369 | 12226 ± 22 | 701 ± 36 |

From Table2, we can see an obvious difference of decay fraction of $f_0(980)\pi^+$ between BABAR and CLEO-c. E687 used about 700 events and the E687 model did not take $f_0(1370)\pi^+$ into account. For CLEO-c, about 14400 events with purity about 84.9% were selected with single tag method. The analysis of BARBAR used about 100000 events with purity about 95%. In this analysis with double tag method, we can get a nearly background free data sample, that will be good to perform the amplitude analysis.

# 2 Data Set and Monte Carlo Samples

We use 3.195 $fb^{-1}$ data set collected at $E_{cm}$ = 4.178$GeV$ by BESIII detector in 2016. Both data sample and Monte Carlo samples are reconstructed under BOSS7.0.3. All samples were generated with run-dependent $E_{cm}$ [13], except for the Bhabha, $\mu - pair$ and Two-photon fusion events. For these three types of events, we used a constant $E_{cm}$ at 4178.37$MeV$ which is twice of a luminosity-weighted average of the measured beam energy in the center-of-mass frame. Totally 40 rounds of generic MC with each round equaling to data size are used for background study, tag efficiencies estimation(rounds 01-30) and input-output check for branching fraction measurement(rounds 31-40). They are available at /besfs3/offline/data/703-1/4180/mc/. For each round of generic MC, the detail component and corresponding size of each Monte Carlo sample are shown in Table 3.

Table 3: Component and corresponding size, assume luminosity = 3195/pb.

| Component | cross section (pb) | Size(M) | directory |
|---|---|---|---|
| $D^0D^0$ | 179 | 0.5719 | D0D0 |
| $D^+D^-$ | 197 | 0.6294 | DpDm |
| $D^{*0}D^0$ | 1211 | 3.8691 | DST0D0 |
| $D^{*+}D^-$ | 1296 | 4.1407 | DSTpDm |
| $D^{*0}D^{*0}$ | 2173 | 6.9427 | DST0DST0 |
| $D^{*+}D^{*-}$ | 2145 | 6.8533 | DSTpDSTm |
| $D_s^+D_s^-$ | 7 | 0.0225 | DsDs |
| $D_s^{*+}D_s^-$ | 961 | 3.0700 | DsSTDs |
| $DD^*\pi^+$ | 383 | 1.2237 | DDSTPIp |
| $DD^*\pi^0$ | 192 | 0.6134 | DDSTPI0 |
| $DD\pi^+$ | 50 | 0.1598 | DDPIp |
| $DD\pi^0$ | 25 | 0.0799 | DDPI0 |
| Component | cross section (nb) | Size(M) | |
| $q\bar{q}$ | 13.8 | 44.0910 | qq |
| $\gamma J/\psi$ | 0.40 | 1.2780 | RR1S |
| $\gamma\psi(2S)$ | 0.42 | 1.3419 | RR2S |
| $\gamma\psi(3770)$ | 0.06 | 0.1917 | RR3770 |
| $\tau\tau$ | 3.45 | 11.0228 | tt |
| $\mu\mu$ | 5.24 | 16.7418 | mm |
| $ee$ | 423.99 | 13.5465(0.01×) | ee |
| $Two - photonfusion$ | 1.7 | 5.4315 | TwoGam |
| HCT | 0.10178 | 0.3252 | HCT |

For the Signal MC, we generate the signal events with one $D_s$ decaying to signal mode using the generator "DIY", in which the parameters are obtained from the fit to data. PHSP MC and Signal MC are used in MC integration required for the amplitude fit. The Signal MC is also used in the input/output check.

# 3 Event Selection

At $E_{cm} = 4.178GeV$, pairs of $D_sD_s^*$ are produced, and the $D_s^*$ decays to either $D_s\gamma$ or $D_s\pi^0$. So the $D_s$ mesons are produced in pairs without additional charged hadrons($K^{\pm}(\pi^{\pm})$). We do not search for the gamma or $\pi^0$ from the $D_s$ decay. These unique $D_s^+D_s^-$ final states provides us an opportunity to employ the double tag method to measure the absolute branching fraction of $D_s$ meson decay. The double tag method also provide us a clean sample to perform an amplitude analysis.

## 3.1 Tracking, PID, $\pi^0/\eta^{(')}$ and $K_S^0$ Reconstruction

$D_s$ candidates are built from $K^{\pm}$, $\pi^{\pm}$, $\pi^0/\eta^{(')}$ and $K_S^0$. The selections of the particles to build $D_S$ candidates are performed with DTagAlg-00-01-05 package with the default setting, which are summarized below.

- Tracking:
  - The properties of charged tracks are determined based on the MDC information. Charged track candidates must satisfy:
    - $|cos\theta| < 0.93$.
    - $|dr| < 1cm$ and $|dz| < 10cm$,
      where $|dr|$ and $|dz|$ are defined as the one reconstructed minus the interaction point.
- Particle ID:
  - Charged tracks are identified as pion or kaon with Particle Identification (PID), which is implemented by combing the information of the energy loss (dE/dx) in MDC and the time-of-flight measured from the TOF system. Kaon and Pion are identified with the requirements that
    - *Prob(K)* $> 0$ and *Prob(K)* $>$ *Prob($\pi$)* for $K$,
    - *Prob($\pi$)* $> 0$ and *Prob($\pi$)* $>$ *Prob(K)* for $\pi$, where *Prob(X)* is the probability of hypothesis X, X can be $\pi$ or $K$.
- $\pi^0/\eta$ selection: $\pi^0/\eta$ candidates are reconstructed through $\pi^0 \to \gamma\gamma(\eta \to \gamma\gamma)$ with package of PioEtaToGGRecAlg.

  The photons are reconstructed as energy showers on the EMC. We require:
  - Minimum energy for barrel showers( $|cos\theta| < 0.8$): $E_{min} > 25MeV/c^2$,

- Minimum energy for endcap showers( $0.86 < |cos\theta| < 0.92$): $E_{min} > 50MeV/c^2$,
- Shower within other $|cos\theta|$ regions are rejected.
- EMC time requirements for events with at least one charged track detected: $0 \leq t \geq 14$(50ns),

Then we perform a constrained fit on the photon pairs to the nominal $\pi^0/\eta$ mass and require:

- The unconstrained invariant mass for $\pi^0$: $0.115 < M(\gamma\gamma) < 0.015GeV/c^2$,
- The unconstrained invariant mass for $\eta$ : $0.490 < M(\eta) < 0.580GeV/c^2$,
- Mass fit: $\chi^2_{1c} < 30$.

- $\eta^{'}$ selection: The $\eta^{'}$ candidates are reconstructed with $\pi^+\pi^-\eta$, the invariant mass for $\pi^+\pi^-\eta$ is required to fall into the range of $[0.938, 0.978]GeV^2$.

- $K^0_S$ selection: $K^0_S$ candidates are reconstructed using VeeVertexAlg package with two opposite charged tracks with requiring:

  - $|cos\theta| < 0.93$
  - $|dz| < 20cm$

  For each pair of tracks, a constrained vertex fit is performed and the track parameters' results are used to get the invariant mass $M(K^0_S)$. Then the decay length of $K^0_S$ is obtained with second vertex fit by the SecondVertexFit package. For $K^0_S$ selection, we require:

  - $0.487GeV/c^2 < M(K^0_S) < 0.511GeV/c^2$.
  - Significance of the $K^0_S$ decay length has two standard deviations.

- $D_s$ selection: The $D_s$ candidates fall into the mass window of $1.87 < m_{D_s} < 2.06GeV/c^2$ and the corresponding $M_{rec}$ satisfied $2.051 < M_{rec} < 2.180GeV/c^2$ are retained for further study. In which, the definition of $M_{rec}$ is

$$M_{rec} = \sqrt{(E_{cm} - \sqrt{p^2_{D_s} + m^2_{D_s}})^2 - |\vec{p}_{cm} - \vec{p}_{D_s}|^2}\ , \tag{5}$$

  where $E_{cm}$ is the energy of initial state, calculated from the beam energy [13], $\vec{p}_{D_s}$ is the momentum of $D_s$ candidate, $m_{D_s}$ is $D_s$ mass quoted from PDG [14] and $\vec{p}_{cm}$ and $\vec{p}_{D_s}$ are four-momentum of initial state and the decay products of a $D_s$ candidate, respectively.

## 3.2 Signal Selection

We use different methods to select events in model independent analysis(Sec. 4.1), amplitude analysis(Sec. 5.1) and branching fraction measurement(Sec. 6.1). And the details are in the corresponding sections.

# 4 Partial Wave Analysis in the Low $K^+K^-$ Mass Region

In the $K^+K^-$ threshold both $a_0(980)$ and $f_0(980)$ can be present, and both resonances have very similar parameters which suffer from large uncertainties. In this section we obtain model-independent information on the $K^+K^-S$ wave by performing a partial wave analysis(PWA) in the $K^+K^-$ threshold region.

## 4.1 Event Selection

After the selection in Set.3, we continue to select signals for model independent partial wave analysis. As PWA need more data events, we decide to use the single-tag method, and only to fully reconstruct one $D_s^+ \to K^+K^-\pi^+$ in each event. Before selecting the best candidate, we vote the candidates with $\pi^\pm(\pi^0)$ whose momentum is less than $0.1GeV$ to remove soft $\pi^\pm(\pi^0)$ from $D^*$ decays. For every candidates of $D_s$ decays, all tracks are added to apply kinematic fitting. Only mass of $D_s$ is constrained.Then we select the candidate with minimum $\chi^2_{1c}$.

## 4.2 Background Analysis

In order to suppress the background, the multiple-variable analysis (MVA) is used. We train MVA methods separately with different sets of variables for the two event categories depending on the $D_s^+$ origin. Sideband region used below is defined as the region of $1.90 < M(D_s) < 1.952GeV$ and $1.985 < M(D_s) < 2.03GeV$, $M(D_s)$ is the invariant mass of $D_s$. And the signal region is $1.952 < M(D_s) < 1.985GeV$. These two categories of events are selected in a $M_{rec} - \Delta M$ 2D plane shown in Fig.2:

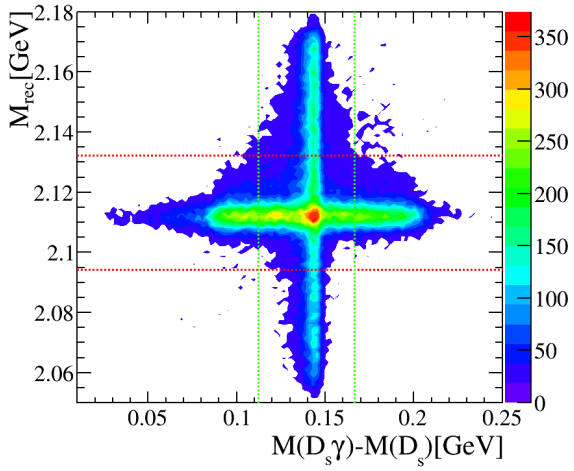


Figure 2: Two dimensional plane of $M_{rec}$ versus $\Delta M \equiv M(D_s^+\gamma) - M(D_s^+)$ from the simulated $D_s^+ \to K^+K^-\pi^+$ decays. The red(green) dashed lines mark the mass window for the $D_s^+$ Cat. #0( Cat. #1) around the $M_{rec}(\Delta M)$ peak.

- Cat. #0: Direct $D_s^+$. We use the following variables whose distributions for signal and background are shown in Fig.3 for generic MC and Fig.4 for data,

  1. $M_{rec}$,
  2. $P_{rest}$, defined as the total momentum of the tracks and neutrals in the rest of event (not part of the $D_s^+ \to K^+K^-\pi^+$ candidate),
  3. $E_\gamma$, defined as the energy of gamma from $D_s^*$.

  From Fig. 3 and Fig.4, we can see that the corresponding distributions of these variables of data and generic MC are roughly consistent.

- Cat. #1: Indirect $D_s^+$. We use the following variables whose distributions for signal and background are shown in Fig.5 for generic MC and Fig.6 for data,

  1. $\Delta M$,
  2. $M_{rec}^{'}$, defined as $M_{rec}^{'} = \sqrt{(E_{cm} - \sqrt{p_{D_s\gamma}^2 + m_{D_s^*}^2})^2 - p_{D_s\gamma}^2}$, with $p_{D_s\gamma}$ as the momentum of the $D_s\gamma$ combination, $m_{D_s^*}$ as the nominal $D_s^*$ mass,
  3. $N_{tracks}$, defined as the total number of tracks and neutrals in an event.

  From Fig. 5 and Fig.6, we can see that the corresponding distributions of these variables of data and generic MC are roughly consistent.

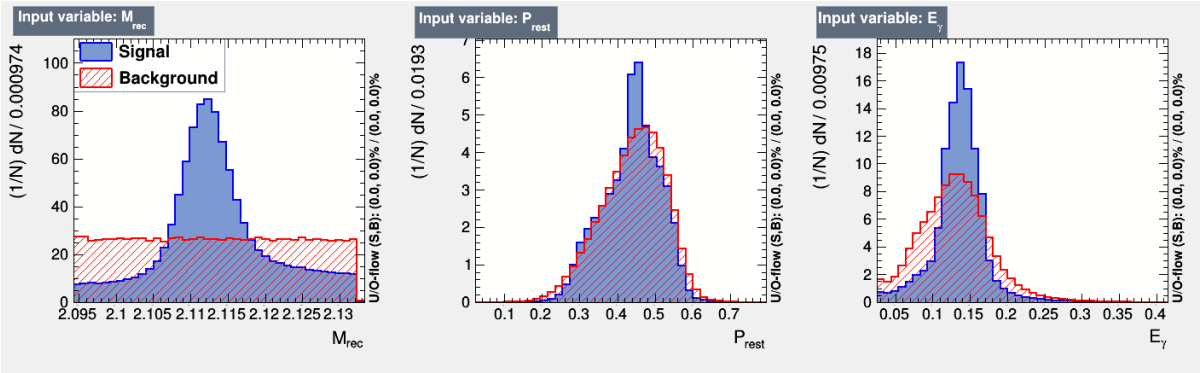


Figure 3: For event Cat. #0, distributions of MVA variables from simulated signal decays and background events.

As the results shown in Fig.7, BDTG training and test samples are well matched. For event Cat. #0 ( Cat. #1 ), the sample with BDTG value larger than 0.33(0.65) is retained for further study.

After applying the BDTG requirement, the background shows no obviously peak around the region of [1.95, 1.982] $GeV$ (Signal region), which are shown in Fig.8. The fit to the signal $D_s$ invariant mass

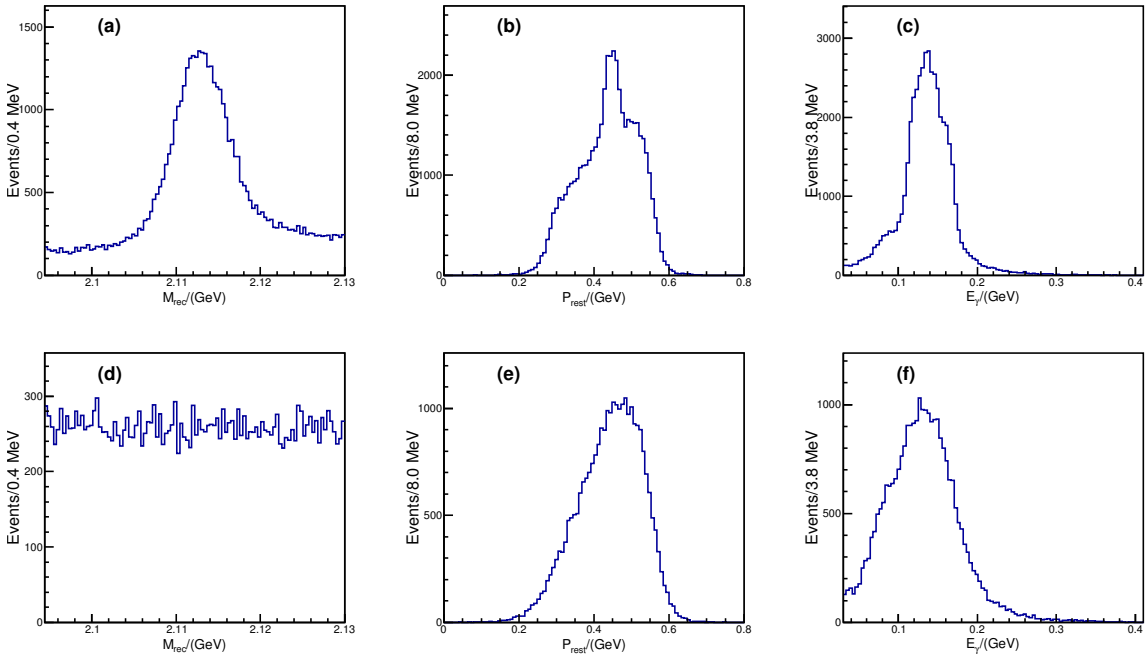


Figure 4: The distribution(Cat. #0) of these three observables ((a) and (d)) $M_{rec}$, ((b) and (e)) $P_{rest}$ and ((c) and (f)) $E_\gamma$ for( (a), (b) and (c)) Signal and ( (d), (e) and (f)) Sideband regions of data.

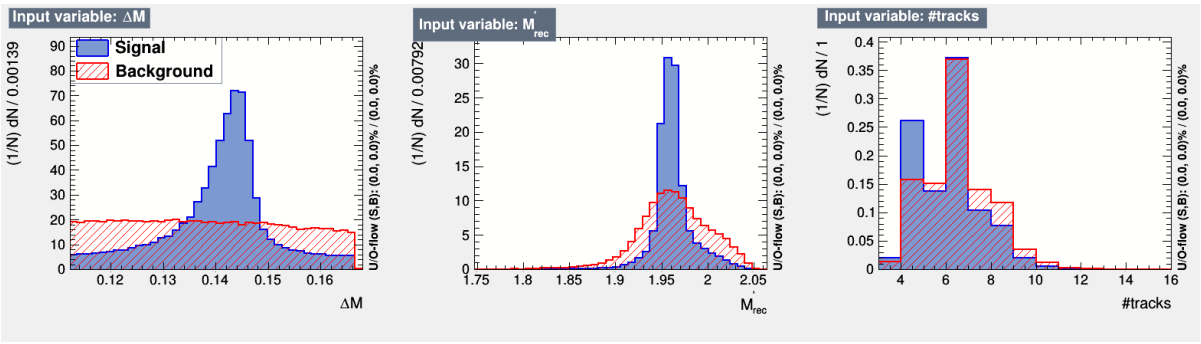


Figure 5: For event Cat. #1, distributions of MVA variables from simulated signal decays and background events.

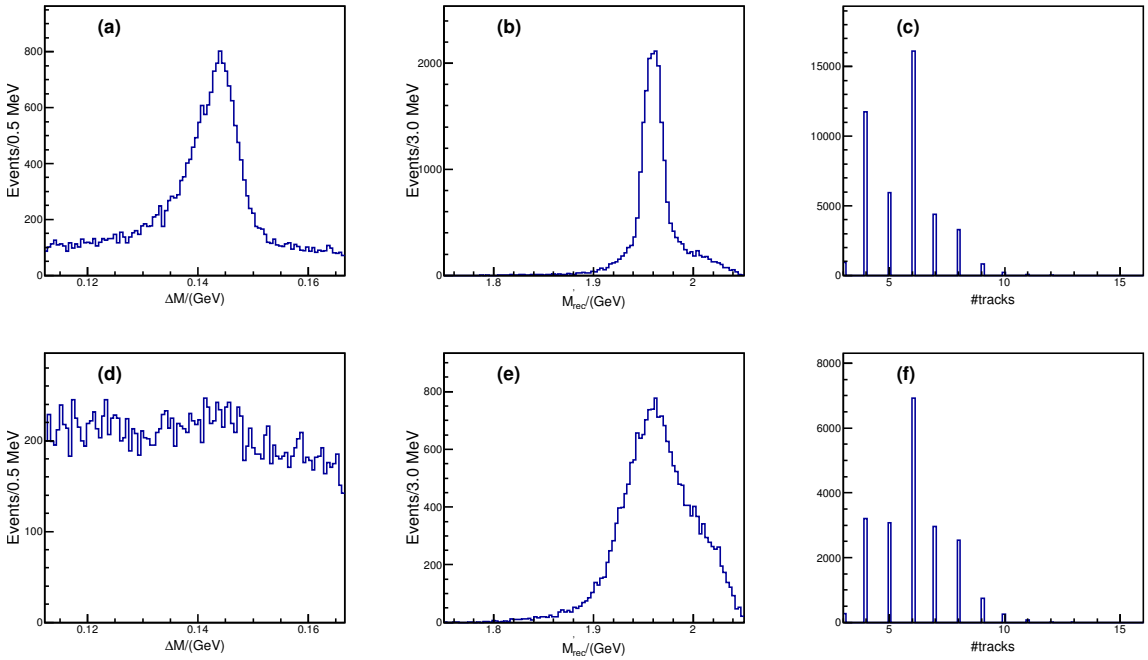


Figure 6: The distribution(Cat. #1) of these three observables ((a) and (d)) $M_{rec}$, ((b) and (e)) $P_{rest}$ and ((c) and (f)) $E_\gamma$ for( (a), (b) and (c)) Signal and ( (d), (e) and (f)) Sideband regions from data are shown.

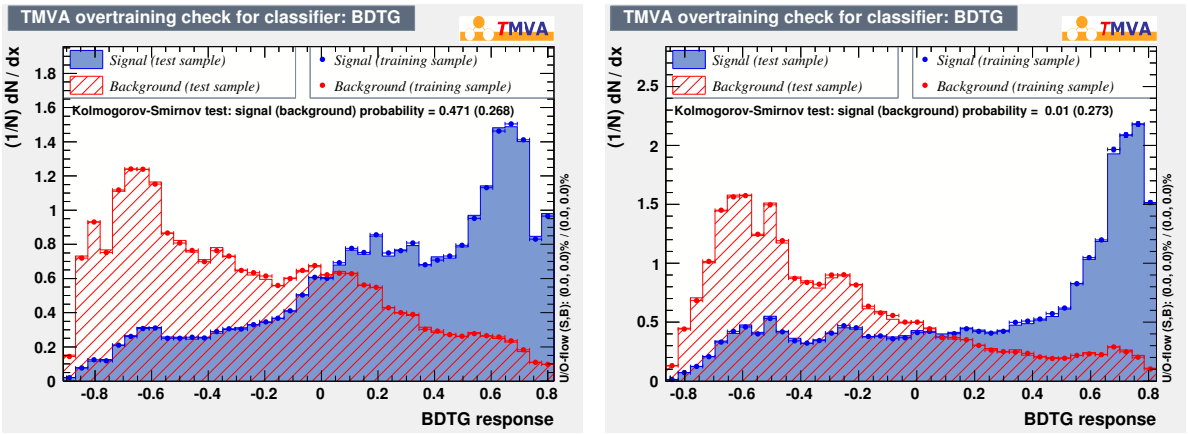


Figure 7: The comparisons between the training and test samples. The plot at left(right) is the comparision of Cat. #0 (Cat. #1).

gives the background yield in Signal region is 73.6 ± 18.7, shown as in Fig.9. In the fit, the signal shape is the MC shape convoluted with a Gaussian function and the background is described with $1^{st}$-order Chebychev polynomial.

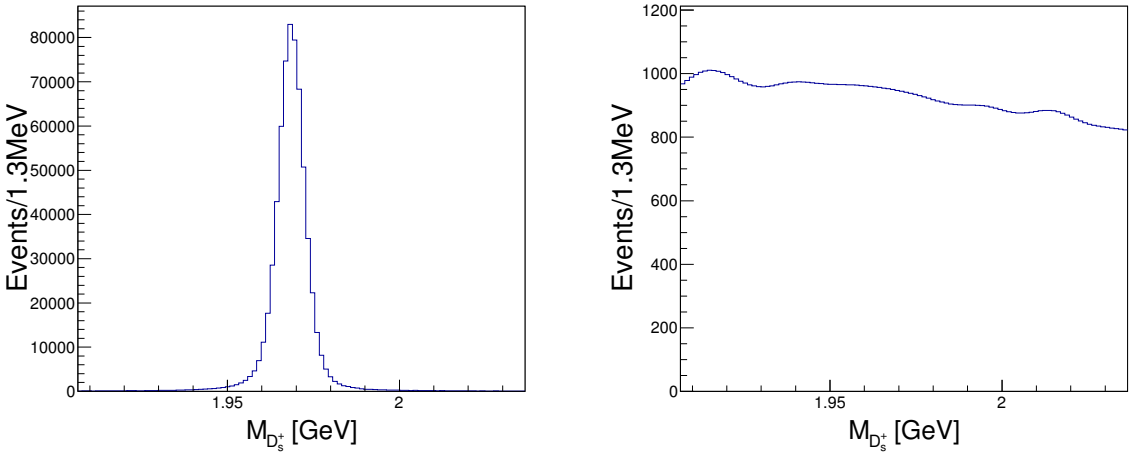


Figure 8: The signal and background distributions from generic MC after BDTG requirement.

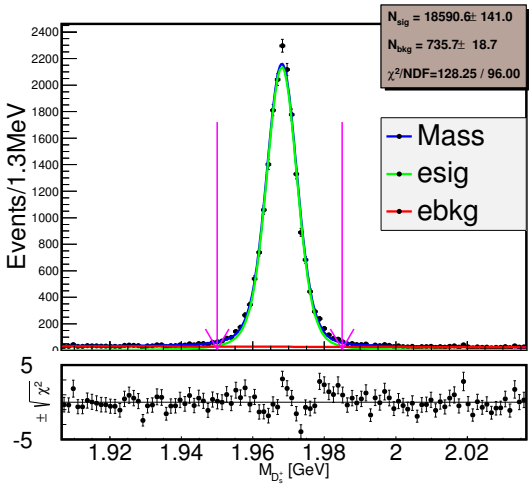


Figure 9: The fit to the signal $D_s$ invariant mass ($M_{D_s}$) spectrum after BDTG requirement, the area between the pink arrows is the signal area of the sample for MIPWA.

The projections of the "sideband"( $1.90 < M(D_s) < 1.95GeV$ and $1.985 < M(D_s) < 2.03GeV$) from data and generic MC with signal events removed are shown in Fig.10. The corresponding plots agree well.

Thus the generic MC sample with signal events removed is used to subtract the background in data.

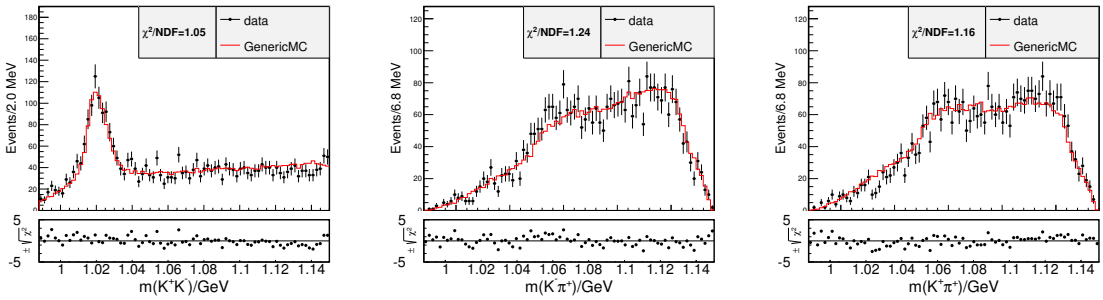


Figure 10: The projections of $m(K^+K^-)$, $m(K^-\pi^+)$, $m(K^+\pi^+)$ from "Sideband" for data(dots with error bars) and generic MC with signal events removed (red histogram) after BDTG requirement.

## 4.3 Partial wave analysis

Let N be the number of events for a given mass interval $I = [m_{K^+K^-}; m_{K^+K^-} + dm_{K^+K^-}]$. We write the corresponding angular distributions in terms of the appropriate spherical harmonic functions as

$$\frac{dN}{d\cos\theta} = 2\pi \sum_{k=0}^{L} \left\langle Y_k^0 \right\rangle Y_k^0(\cos\theta), \tag{6}$$

where $L - 2\ell_{max}$, and $\ell_{max}$ is the maximum orbital angular momentum quantum number required to describe the $K^+K^-$ system at $m_{K^+K^-}$ (e.g. $\ell_{max}$ =1 for S-, P-wave description); $\theta$ is the angle between the $K^+$ direction in the $K^+K^-$ system in the $D_s^+$ rest frame. The normalizations are

$$\int_{-1}^{1} Y_k^0(\cos\theta) Y_j^0(\cos\theta), d\cos\theta = \frac{\delta_{kj}}{2\pi}, \tag{7}$$

and it is assumed that the distribution $\frac{dN}{d\cos\theta}$ has been efficiency corrected and background subtracted. Using this orthogonality condition, the coefficiencies in the expansion are obtained from

$$\left\langle Y_k^0 \right\rangle = \int_{-1}^{1} \frac{dN}{d\cos\theta} d\cos\theta, \tag{8}$$

where the integral is given, to a good approximation, by $\sum_{n=1}^{N} Y_k^0(\cos\theta_n)$, where $\theta_n$ is the value of $\theta$ for the $n$-th event.

Fig.11 shows the $K^+K^-$ mass spectrum up to 1.15 GeV weighted by $Y_k^0(\cos\theta) = \sqrt{(2k+1)/(4\pi)} P_k(\cos\theta)$ for k=0, 1, and 2, where $P_k$ is the Legendre polynomial function of order $k$. These distributions are corrected for efficiency and phase space, and background is subtracted using background from generic MC after BDTG requirement.

The number of events N for the mass interval $I$ can be expressed also in terms of the partial-wave amplitudes describing the $K^+K^-$ system. Assuming that only S- and P-wave amplitudes are necessary in this limited region, we can write:

$$\frac{dN}{d\cos\theta} = 2\pi \left| S\, Y_0^0(\cos\theta) + P Y_1^0(\cos\theta) \right|^2. \tag{9}$$

By comparing Eq. 6 and 9, we obtain

$$\begin{aligned}\sqrt{4\pi}\left\langle Y_0^0\right\rangle &= |S|^2 + |P|^2\,,\\ \sqrt{4\pi}\left\langle Y_2^0\right\rangle &= \tfrac{2}{\sqrt{5}}\,|P|^2\,,\end{aligned} \tag{10}$$

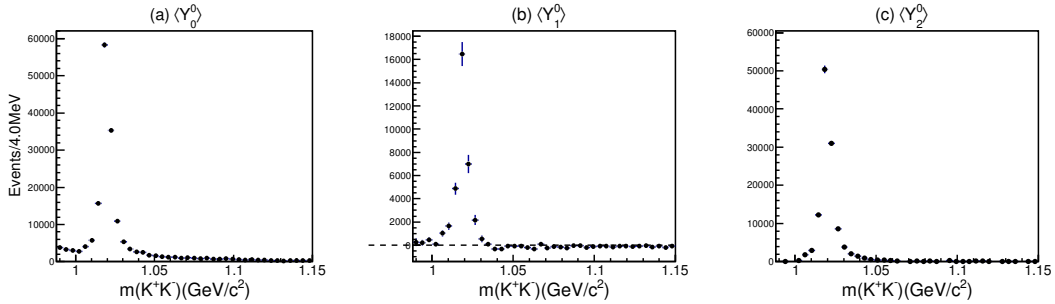


Figure 11: $K^+K^-$ mass spectrum in the threshold region weighted by (a) $Y_0^0$, (b) $Y_1^0$ and (c) $Y_2^0$, corrected for efficiency and phase space, and background subtracted.

The above system of equations can be solved in each interval of $K^+K^-$ invariant mass for $|S|$ and $|P|$ and the resulting distributions are shown in Fig.12.

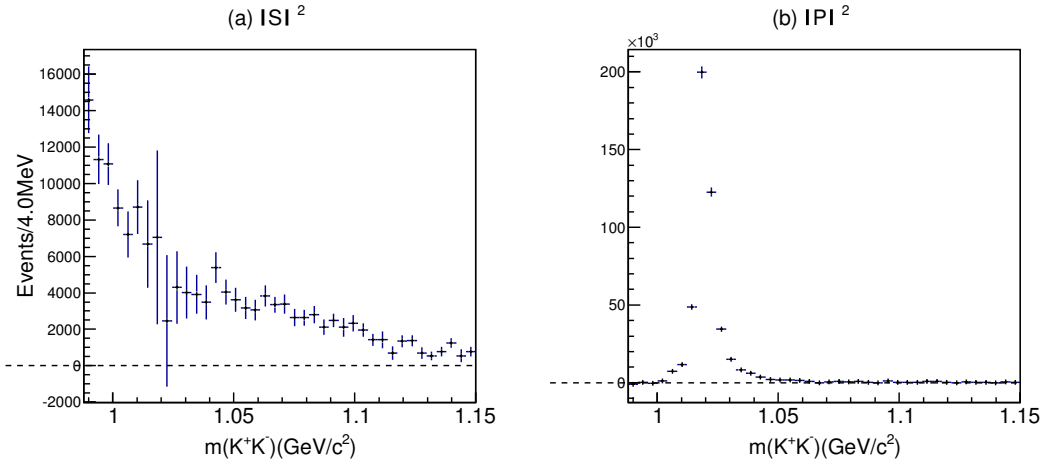


Figure 12: Squared (a) S- and (b) P-wave amplitudes

## 4.4 S-wave parameterization at the $K^+K^-$ threshold

We empirically parameterize the $f_0(980)$ with the following function:

$$A_{f_0(980)/a_0(980)} = \frac{1}{m_0^2 - m^2 - im_0\Gamma_0\rho_{KK}}, \tag{11}$$

where $\rho_{KK} = 2p/m$, and obtain the following parameter values:

$$\begin{aligned} m_0 &= (0.919 \pm 0.006_{stat})GeV,\\ \Gamma_0 &= (0.272 \pm 0.040_{stat})GeV. \end{aligned} \tag{12}$$

The errors are statistical only. The fit result are shown in Fig.13.

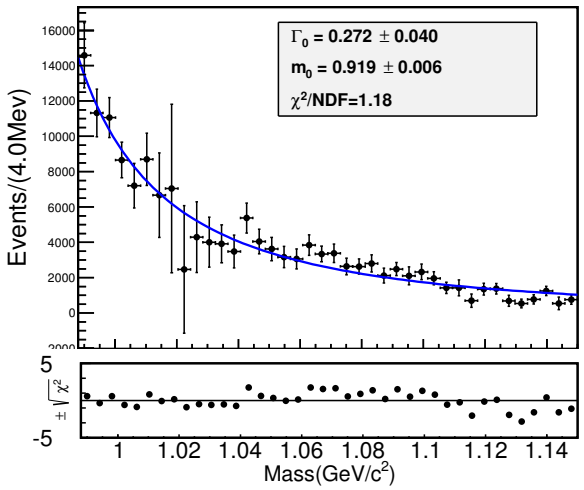


Figure 13: Fit of squared S-wave amplitudes. The curves result from the fit described in the text.

# 5 Amplitude Analysis

## 5.1 Event Selection

After $K^{\pm}$, $K^0_S$, $\pi^{\pm}$ and $\gamma$ are identified in Sec. 3, hadronic $D_s$ decays can be reconstructed with the DTag package. 8 tag modes are used:

$D_s^- \to K^+K^-\pi^-$, $D_s^- \to K^0_S K^-$, $D_s^- \to K^0_S K^-\pi^+\pi^-$, $D_s^- \to K^-\pi^+\pi^-$, $D_s^- \to K^0_S K^+\pi^-\pi^-$, $D_s^- \to \pi^+\pi^-\pi^-$, $D_s^- \to \eta^{'}_{\pi^+\pi^-\eta_{\gamma\gamma}}$, $D_s^- \to K^+K^-\pi^-\pi^0$.

With the tagged $D_s$ meson, the signal $D_s$ is reconstructed with the remaining good tracks and good showers. The momentum of $\pi^{\pm}(\pi^0)$ is required to be larger than $100MeV/c^2$ to suppress the background of $D^* \to D\pi$. Only the $D_s$ candidate with invariant mass falls into $[1.87, 2.06]GeV/c^2$ are selected.

For every candidate of $D_s$ decays, all tracks at signal side and tag side as well as gamma from $D_s^*$ are added to apply kinematic fitting. 5 constrains are added in kinematic fitting: four-momentum of $D_sD_s^*$, mass of $D_s^*$. Then we select the candidate with minimum $\chi^2_{5c}$.

The candidates satisfy:

- $m_{sig}$ and $m_{tag}$ falls in the mass regions shown in Table4.
- $\chi^2_{5c} < 200$

are retained for amplitude analysis, where $m_{sig}$ and $m_{tag}$ refer to mass of $D_s$ at signal side and tag side respectively.

Table 4: The mass windows for each tag mode. The mass windows use the results in Ref. [15]

| Tag mode | Mass window(GeV) |
|---|---|
| $D_s^- \to K^0_S K^-$ | [1.948, 1.991] |
| $D_s^- \to K^+K^-\pi^-$ | [1.900, 2.030] |
| $D_s^- \to K^+K^-\pi^-\pi^0$ | [1.947, 1.982] |
| $D_s^- \to K^0_S K^-\pi^+\pi^-$ | [1.958, 1.980] |
| $D_s^- \to K^0_S K^+\pi^-\pi^-$ | [1.953, 1.983] |
| $D_s^- \to \pi^-\pi^-\pi^+$ | [1.952, 1.984] |
| $D_s^- \to \pi^-\eta^{'}_{\pi^+\pi^-\eta_{\gamma\gamma}}$ | [1.940, 1.996] |
| $D_s^- \to K^-\pi^+\pi^-$ | [1.953, 1.983] |

## 5.2 Background Analysis

We use generic MC to estimate the background. The background and signal shape of generic MC is shown in Fig.14. According to the luminosities of the data and the generic MC, after scaling the

background sample to the data size, the background yields in Signal region is 17.2. Then the fit to the signal $D_s$ invariant mass ($m_{sig}$) spectrum gives the background yield in Signal region is $18.1 \pm 5.1$, shown as in Fig.15. The background level in MC is then consistent with the data. In the fit, the signal shape is the MC shape convoluted with a Gaussian function and the background is the MC shape.

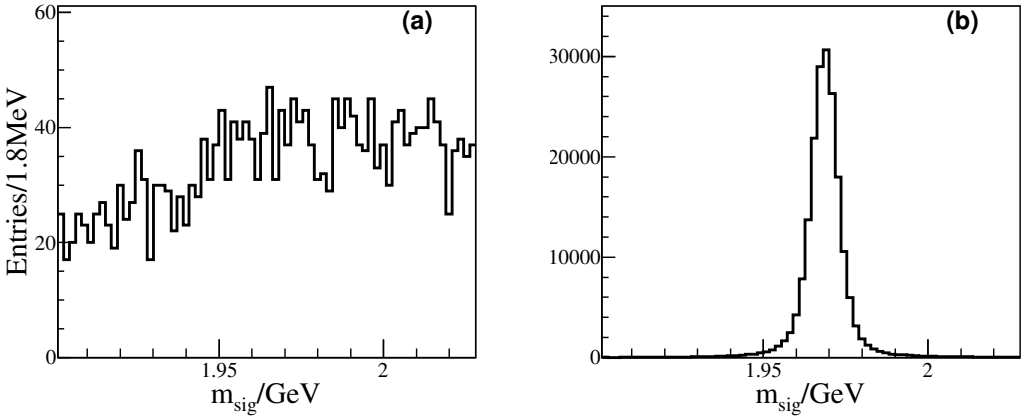


Figure 14: The background and signal shape of generic MC(round 01-40)

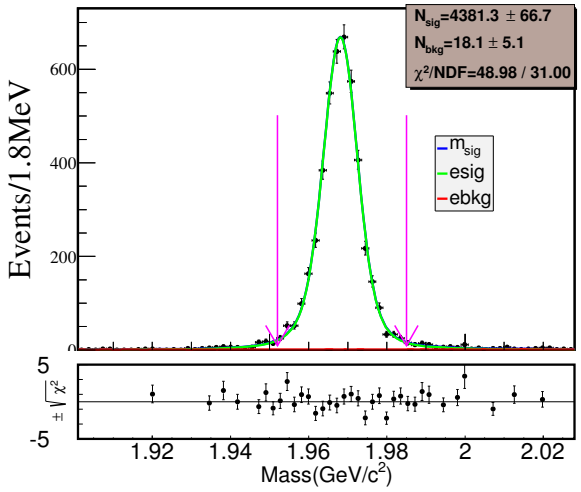


Figure 15: The fit to $m_{sig}$ for data after selections, the area between the purple arrows is the signal area of the sample for the amplitude analysis.

## 5.3 Fit Method

The method used in amplitude analysis is the same as the Ref. [16]. In this section, we briefly review the amplitude analysis method used in this analysis.

The relative magnitudes and phases of the partial waves and the mass and width of intermediate resonances are determined by a maximum-likelihood fit to the data selected. The formulas are constructed

with covariant tensors [17].

Since there are three final state particles, only one possible resonant state is allowed in any intermediate process. Thus the amplitude of the $n^{th}$ intermediate state ($A_n$) is,

$$A_n = P_n S_n F_n^r F_n^D, \tag{13}$$

where $S_n$ and $F_n^{r(D)}$ are the spin factor and the Blatt-Weisskopf barriers of the intermediate state (the $D_s$ meson), respectively. $P_n$ is the propagator of the intermediate resonance.

The total amplitude $M$ is then the coherent sum of the amplitudes of intermediate processes, $M = \sum c_n A_n$, where $c_n = \rho_n e^{i\phi_n}$, is the corresponding complex coefficient. The magnitude $\rho_n$ and phase $\phi_n$ are determined by the amplitude analysis. The signal probability density function(PDF) $f_S(p_j)$ is given by

$$f_S(p_j) = \frac{\epsilon(p_j)\left|M(p_j)\right|^2 R_3(p_j)}{\int \epsilon(p_j)\left|M(p_j)\right|^2 R_3(p_j)\, dp_j}, \tag{14}$$

where $\epsilon(p_j)$ is the detection efficiency parameterized in terms of the final four-momenta $p_j$. The index $j$ refers to the different particles in the final states. $R_3(p_j)dp_j$ is the standard element of the three-body phase space. The normalization integral is determined by a MC technique,

$$\int \epsilon(p_j)\left|M(p_j)\right|^2 R_3(p_j)\, dp_j \approx \frac{1}{N_{MC}} \sum_{k_{MC}}^{N_{MC}} \frac{\left|M(p_j^{k_{MC}})\right|^2}{\left|M^{gen}(p_j^{k_{MC}})\right|^2}, \tag{15}$$

where $k_{MC}$ is the index of the $k_{MC}^{th}$ event of the MC sample and $N_{MC}$ is the number of the selected MC events. $M^{gen}(p_j)$ is the PDF used to generate the MC samples in MC integration. Firstly, the PHSP MC are used in MC integration. $M^{gen}(p_j)$ is a constant overall the phase space. Then with the result obtained from the fit to data, the signal MC is then generated and used in MC integration. In this analysis, a PHSP MC sample with about 6 million events and a signal MC sample with about 2 million events are used in the normalization integral calculation using PHSP MC and signal MC respectively. In the numerator of Eq.14, $\epsilon(p_j)$ is independent of the fitted variables, so it is regarded as a constant term in the fit. Considering the bias caused by particle identification(PID) and tracking efficiency differences between data and MC, we introduce $\gamma_\epsilon$ to correct this bias:

$$\gamma_\epsilon = \prod_i \frac{\epsilon_{i,data}(p_i)}{\epsilon_{i,MC}(p_i)}, \tag{16}$$

where $i$ denotes the three daughter particles. The values of $\frac{\epsilon_{i,data}(p_i)}{\epsilon_{i,MC}(p_i)}$ used in this analysis are from the references [21] and [22].

Since there is only about 0.4% background in the data sample, the contribution from the background is ignored in the likelihood calculation:

$$\ln L = \sum_k^{N_{data}} \ln f_S(p_j^k), \tag{17}$$

where $N_{data}$ is the number of candidate events in data.

### 5.3.1 Propagator

For a decay process $a \to bc$, $s_{a/b/c}$ is denoted to be the invariant mass square of the particle a/b/c, $r_a = p_b - p_c$, and q is denoted as the magnitude of the momentum of daughter particle in the rest system of a

$$q = \sqrt{\frac{(s_a + s_b + s_c)^2}{4s_a} - s_b}. \tag{18}$$

Then for $K^*(892)^0$, $\phi(1020)^0$, $K_0^*(1430)^0$ and $f_0(1710)$, they are parameterized as a RBW,

$$\begin{aligned} P &= \frac{1}{(m_0^2 - s_a) - im_0\Gamma(m)}, \\ \Gamma(m) &= \Gamma_0 \left(\frac{q}{q_0}\right)^3 \left(\frac{m_0}{m}\right) \left(\frac{X_L(q)}{X_L(q_0)}\right)^2, \end{aligned} \tag{19}$$

where $m_0$ and $\Gamma_0$ are the mass and the width of the intermediate resonances, and are fixed to the PDG values [2] except the mass and the width of $f_0(1370)$. The mass and width of $f_0(1370)$ are fixed to Ref. [18]. And $q_0$ in Eq. 19 indicates the value of $q$ when $s_a = m_0^2$, L denotes the angular momenta and $X_L(q)$ is defined as:

$$\begin{aligned} X_{L=0}(q) &= 1, \\ X_{L=1}(q) &= \sqrt{\frac{2}{z^2+1}}, \\ X_{L=2}(q) &= \sqrt{\frac{13}{9z^4+3z^2+1}}, \end{aligned} \tag{20}$$

where $z = qR$, the R is the effective radius of the intermediate state or $D_s$ meson and set to $3.0GeV^{-1}$ for intermediate states and $5.0GeV^{-1}$ for $D_s$ meson [16], respectively. This value R is a typical value used by $D$ physics and we will also vary this value as a resource of systematical uncertainties.

$K_0^*(1430)^0$ is parameterized with Flatte formula:

$$P_{K_0^*(1430)^0} = \frac{1}{M^2 - s - i(g_1\rho_{K\pi}(s) + g_2\rho_{\eta' K}(s))}, \tag{21}$$

where $s$ is the $K^-\pi^+$ invariant mass squared, $\rho_{K\pi}(s)$ and $\rho_{\eta' K}(s)$ are Lorentz invariant PHSP factor, and $g_{1,2}$ are coupling constants to the corresponding final state. The parameters of $K_0^*(1430)^0$ are fixed to values measured by CLEO [19]. For resonance $f_0(980)$ and $a_0(980)$, as is discussed in Sec. 1.1, we take $f_0(980)$ and $a_0(980)$ as a whole, and the RBW form Eq.11 is used to describe the propagator and the values of parameters are fixed to the values in Eq.12 obtained from the model independent partial wave analysis section(Sec. 4.4).

### 5.3.2 Blatt-Weisskopf Barriers

The Blatt-Weisskopf barriers are given by

$$\begin{aligned} F_n &= 1, \qquad (S\ wave), \\ F_n &= \sqrt{\tfrac{z_0^2+1}{z^2+1}}, \quad (P\ wave), \\ F_n &= \sqrt{\tfrac{z_0^4+3z_0^2+9}{z^4+3z^2+9}}, \quad (D\ wave), \end{aligned} \tag{22}$$

where $z_0$ are $qR$ and $q_0R$, respectively.

### 5.3.3 Spin Factors

As the limit of the phase space, we only consider the states with angular momenta no more than 2. Considering a two-body decay, the spin projection operators are defined as

$$\begin{aligned} &P^0(a) = 1, \qquad (S\ wave), \\ &P^{(1)}_{\mu\mu'}(a) = -g_{\mu\mu'} + \frac{p_{a,\mu}p_{a,\mu'}}{p_a^2}, (P\ wave), \\ &P^2_{\mu\nu\mu'\nu'}(a) = \tfrac{1}{2}(P^{(1)}_{\mu\mu'}(a)P^{(1)}_{\nu\nu'}(a) + P^{(1)}_{\mu\nu'}(a)P^{(1)}_{\nu\mu'}(a)) + \tfrac{1}{3}P^{(1)}_{\mu\nu}(a)P^{(1)}_{\mu'\nu'}(a),\ (D\ wave). \end{aligned} \tag{23}$$

The covariant tensors are given by

$$\begin{aligned} \tilde{t}^{(0)}(a) &= 1, \qquad (S\ wave), \\ \tilde{t}^{(1)}_{\mu}(a) &= -P^{(1)}_{\mu\mu'}(a)r^{\mu'}, \qquad (P\ wave), \\ \tilde{t}^{(2)}_{\mu\nu}(a) &= P^{(2)}_{\mu\nu\mu'\nu'}(a)r_a^{\mu'}r_a^{\nu'}, \ (D\ wave). \end{aligned} \tag{24}$$

Then the spin factor for $D_s \to aX$ and then $a \to bc$ is( $a$ refers to the intermediate resonance),

$$\begin{aligned} S_n &= 1, \qquad (S\ wave), \\ S_n &= \tilde{T}^{(1)\mu}(D_s)\tilde{t}^{(1)}_{\mu}(a), \quad (P\ wave), \\ S_n &= \tilde{T}^{(2)\mu}(D_s)\tilde{t}^{(2)}_{\mu}(a), \quad (D\ wave), \end{aligned} \tag{25}$$

where the $\tilde{T}^{(1)\mu}(D_s)(\tilde{T}^{(2)\mu}(D_s))$ and $\tilde{t}^{(1)}_{\mu}(a)(\tilde{t}^{(2)}_{\mu}(a))$ are the same defined in Ref. [17].

## 5.4 Fit Fraction

The fit fractions of the individual amplitudes are calculated according to the fit results and are compared to the other measurements. In the calculation, a phase space(PHSP) MC with neither detector acceptance nor resolution involved is used. The fit fraction for an amplitude is defined as

$$FF(n) = \frac{\sum_{k=1}^{N_{gen}} |A_n|^2}{\sum_{k=1}^{N_{gen}} \left|M(p_j^k)\right|^2}, \tag{26}$$

where $N_{gen} = 2000000$, is the number of the PHSP MC events at generator level.

To estimate the statistical uncertainties of the fit fractions, we repeat the calculation of fit fractions by randomly varying the fitted parameters according to the error matrix. Then, for each amplitude , we fit the resulting distribution with a Gaussian function, whose width gives the corresponding statistical uncertainty.

## 5.5 Fit Result

The Dalitz plot of $m^2(K^+K^-)$ versus $m^2(K^-\pi^+)$ is shown in Fig.16. In the plot, we can see a clear peak of $K^*(892)^0$ and $\phi(1020)^0$. In the fit, the magnitude and phase of the amplitude $D_s^+ \to K^*(892)^0K^+$ is fixed to 1.0 and 0.0, and the magnitudes and phases of the amplitudes are allowed to float.

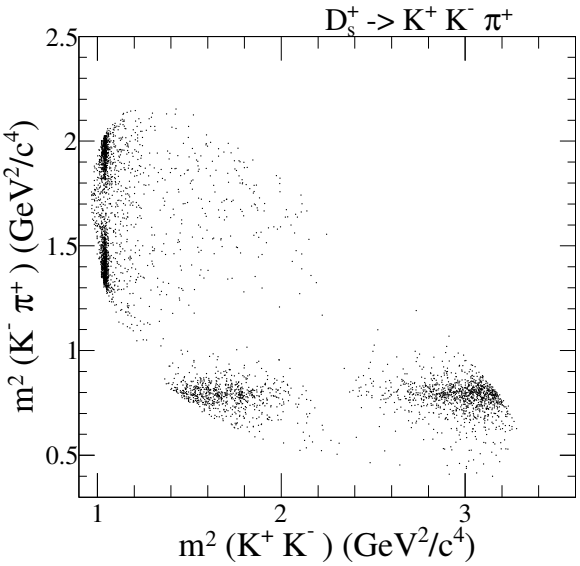


Figure 16: The plot of $m^2(K^-\pi^+)$ versus $m^2(K^+K^-)$ after event selection.

With the requiring the statistical significance larger than 5 standard deviations, there are 6 intermediate process, $D_s^+ \to \bar{K}^*(892)^0K^+$, $D_s^+ \to \phi(1020)\pi^+$, $D_s^+ \to f_0(980)\pi^+/a_0(980)\pi^+$, $D_s^+ \to \bar{K}_0^*(1430)^0K^+$, $D_s^+ \to f_0(1370)\pi^+$, $D_s^+ \to f_0(1710)\pi^+$ are retained in final result. The statistical significance of the three amplitudes in final result are also checked. With one amplitude dropped and the fit repeated, compared with the nominal fit the likelihood shift($\Delta \ln L$) and the number of freedom degree shift($\Delta n_{par}$) are then corresponding to the statistical significance. The detail $\Delta \ln L$, $\Delta n_{par}$, and the statistical significance for each amplitude are listed in Table 5. We also tested some other intermediate resonances. With each tested amplitude added and fit repeated, we get the corresponding likelihood shift($\Delta \ln L$), the number of freedom degree shift($\Delta n_{par}$) and the statistical significance. And the results are listed in Table 6. As the statistical significances of the amplitudes listed in Table 6 are $< 5$, we did not retain them in the nominal fit.

The detail magnitudes, phases and fit fractions for the six amplitudes are listed in Table 7.

The Dalitz plot projections are shown in Fig.17.

The goodness of the nominal fit is $\chi^2 = 290.1/280 = 1.04$.

Table 5: The $\Delta \ln L$, $\Delta n_{par}$, and the statistical significance for each amplitude

| Amplitude | $\Delta \ln L$ | $\Delta n_{par}$ | Stat. significance |
|---|---|---|---|
| $D_s^+ \to \bar{K}^*(892)^0 K^+$ | 1959.3 | 2 | >20 |
| $D_s^+ \to \phi(1020)\pi^+$ | 2303.3 | 2 | >20 |
| $D_s^+ \to f_0(980)\pi^+ / a_0(980)\pi^+$ | 270.5 | 2 | >20 |
| $D_s^+ \to \bar{K}_0^*(1430)^0 K^+$ | 39.4 | 2 | 8.6 |
| $D_s^+ \to f_0(1710)\pi^+$ | 44.7 | 2 | 9.2 |
| $D_s^+ \to f_0(1370)\pi^+$ | 22.5 | 2 | 6.4 |

Table 6: The $\Delta \ln L$, $\Delta n_{par}$, and the statistical significance for tested amplitudes

| Amplitude | $\Delta \ln L$ | $\Delta n_{par}$ | Stat. significance |
|---|---|---|---|
| $D_s^+ \to f_0(1500)\pi^+$ | 0.8 | 2 | 0.8 |
| $D_s^+ \to \phi(1680)\pi^+$ | 1.8 | 2 | 1.4 |
| $D_s^+ \to f_2(1270)\pi^+$ | 4.5 | 2 | 2.5 |
| $D_s^+ \to f_2(1525)\pi^+$ | 0.2 | 2 | 0.2 |
| $D_s^+ \to \bar{K}_1^*(1410)^0 K^+$ | 4.8 | 2 | 2.6 |
| $D_s^+ \to \bar{K}_1^*(1680)^0 K^+$ | 0.1 | 2 | 0.1 |
| $D_s^+ \to \bar{K}_2^*(1430)^0 K^+$ | 2.8 | 2 | 1.9 |
| non-resonance | 6.4 | 2 | 3.1 |

Table 7: The magnitudes, phases and fit fractions for the six amplitudes

| Amplitude | Magnitude | Phase | Fit fractions(%) |
|---|---|---|---|
| $D_s^+ \to \bar{K}^*(892)^0 K^+$ | 1.0(fixed) | 0.0(fixed) | 48.3±0.9 |
| $D_s^+ \to \phi(1020)\pi^+$ | 1.09±0.02 | 6.22±0.07 | 40.5±0.7 |
| $D_s^+ \to f_0(980)\pi^+ / a_0(980)\pi^+$ | 2.88±0.14 | 4.77±0.07 | 19.3±1.7 |
| $D_s^+ \to \bar{K}_0^*(1430)^0 K^+$ | 1.26±0.14 | 2.91±0.20 | 3.0±0.6 |
| $D_s^+ \to f_0(1710)\pi^+$ | 0.79±0.08 | 1.02±0.12 | 1.9±0.4 |
| $D_s^+ \to f_0(1370)\pi^+$ | 0.58±0.08 | 0.59±0.17 | 1.2±0.4 |

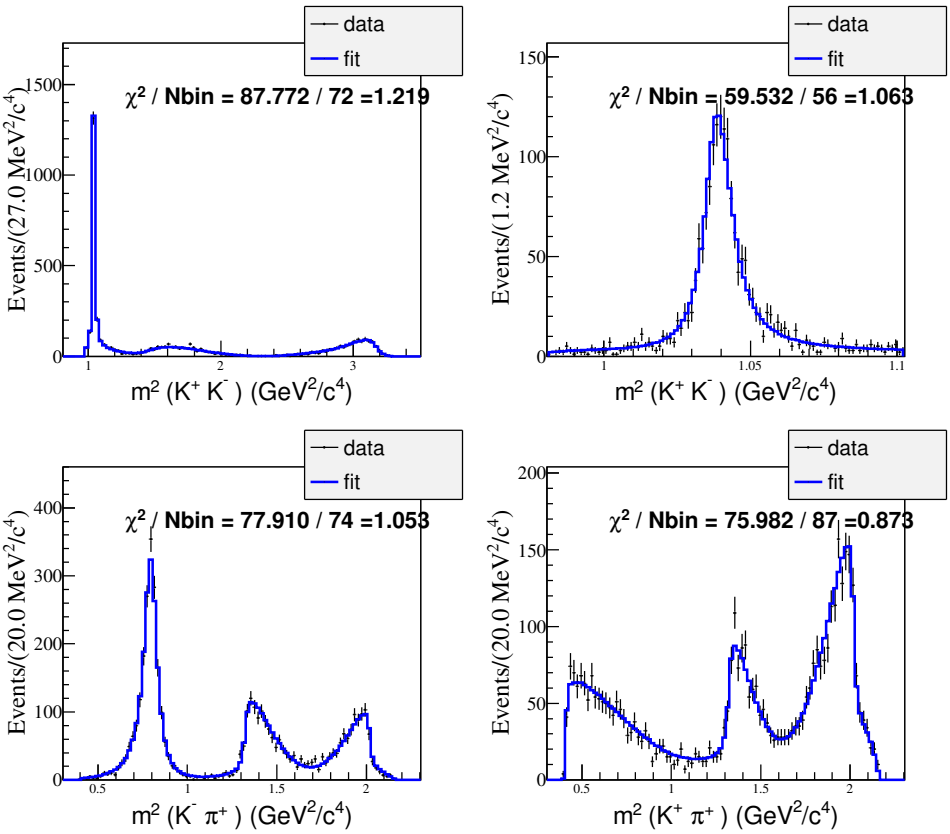


Figure 17: $D_s^+ \to K^+K^-\pi^+$: Dalitz plot projections from the nominal fit. The data are represented by points with error bars, the fit results by the histograms.

Table 8: The results of pull distribution checks for the magnitudes, phases and fit fractions for different amplitudes.

| Amplitude | Phase | | Magnitude | | Fit fraction | |
|---|---|---|---|---|---|---|
| | mean | width | mean | width | mean | width |
| $D_s^+ \to \bar{K}^*(892)^0 K^+$ | | | | | -0.13±0.04 | 0.98±0.03 |
| $D_s^+ \to \phi(1020)\pi^+$ | -0.04±0.05 | 1.00±0.03 | 0.07±0.04 | 0.95±0.03 | 0.01±0.04 | 0.95±0.03 |
| $D_s^+ \to f_0(980)\pi^+/a_0(980)\pi^+$ | -0.07±0.05 | 1.01±0.03 | 0.07±0.05 | 1.10±0.04 | 0.02±0.05 | 1.14±0.04 |
| $D_s^+ \to \bar{K}_0^*(1430)^0 K^+$ | 0.00±0.05 | 1.11±0.04 | 0.14±0.04 | 0.95±0.03 | 0.10±0.04 | 0.99±0.03 |
| $D_s^+ \to f_0(1710)\pi^+$ | 0.00±0.04 | 0.98±0.03 | 0.08±0.04 | 0.97±0.03 | 0.01±0.04 | 0.99±0.03 |
| $D_s^+ \to f_0(1370)\pi^+$ | -0.11±0.05 | 1.10±0.04 | 0.21±0.04 | 0.99±0.03 | 0.15±0.04 | 0.98±0.03 |

## 5.6 Systematic Uncertainties

Systematic uncertainties take in account:

- I Variation of resonance masses and widths within $1\sigma$ error.
  - For $f_0(980)/a_0(980)$, the mass and width are shifted within errors from Eq.12 in Sec. 4.4.
  - For $f_0(1370)$, the mass and width are shifted within errors from [18].
  - For other states, errors used here are taken from PDG [2].
- II Variation of the effective radius of Blatt-Weisskopf Barrier within the range $[1.0, 5.0]\,GeV^{-1}$ for intermediate resonances and $[3.0, 7.0]\,GeV^{-1}$ for $D_s$ meson.
- III Fit bias. The possible bias is given by the result from pull distribution check. With the results obtained from the fit, the signal MC samples are generated with the same size of the data. In this analysis, 300 MC samples with the size equaling to data are used to perform the pull distribution check. The results are listed in Table 8. The corresponding plots are shown in Fig.18, Fig.19 and Fig.20.
- IV Experimental effects. The experimental effects are related to the acceptance difference between MC and data caused by PID and tracking efficiencies, that is $\gamma_\epsilon$ in Eq. 16. To estimate the uncertainties caused by $\gamma_\epsilon$, the amplitude fit is performed varying PID and tracking efficiencies according to their uncertainties.

Thus, the detail results of the systematic uncertainties are summarized in Table 9. The final results of the amplitude analysis are then listed in Table 10.

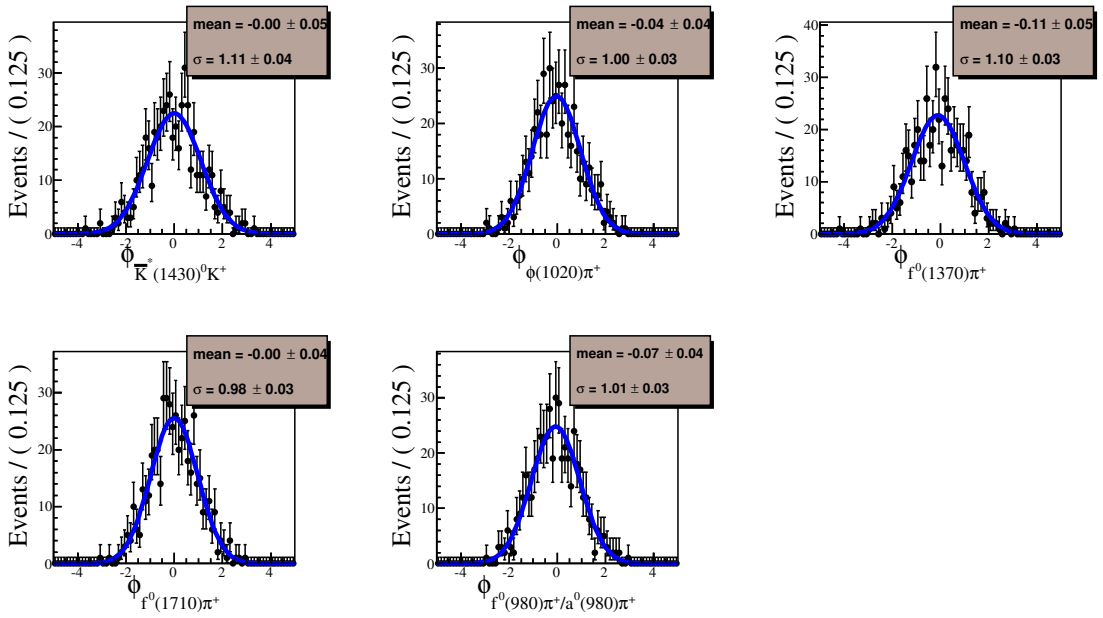


Figure 18: The pull distribution check results for phases of the amplitudes in the nominal fit model.

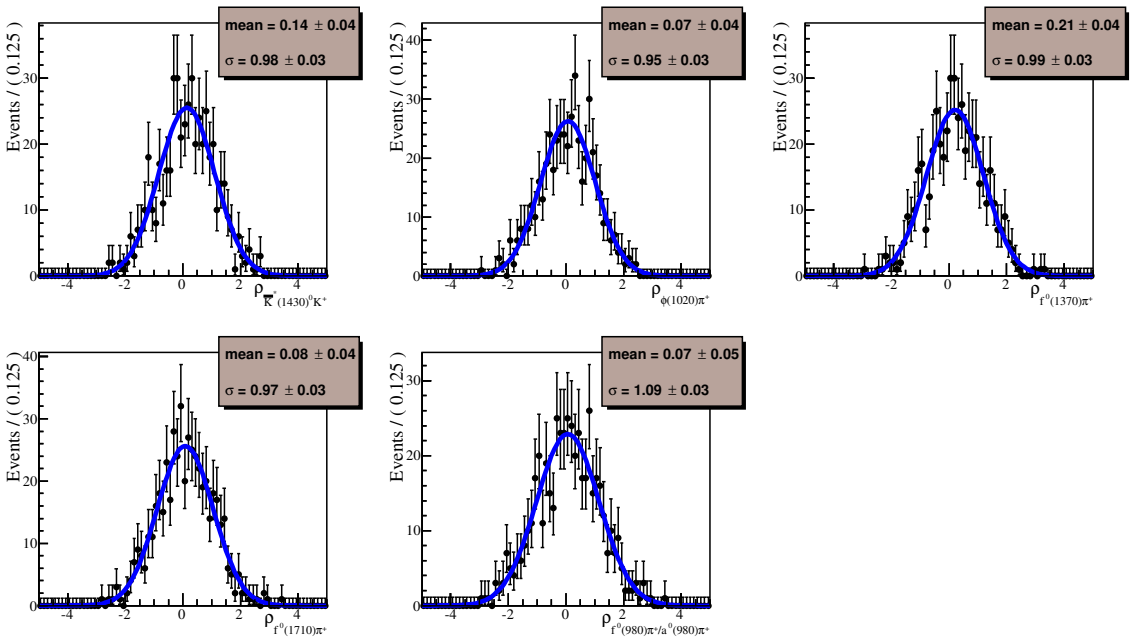


Figure 19: The pull distribution check results for magnitudes of the amplitudes in the nominal fit model.

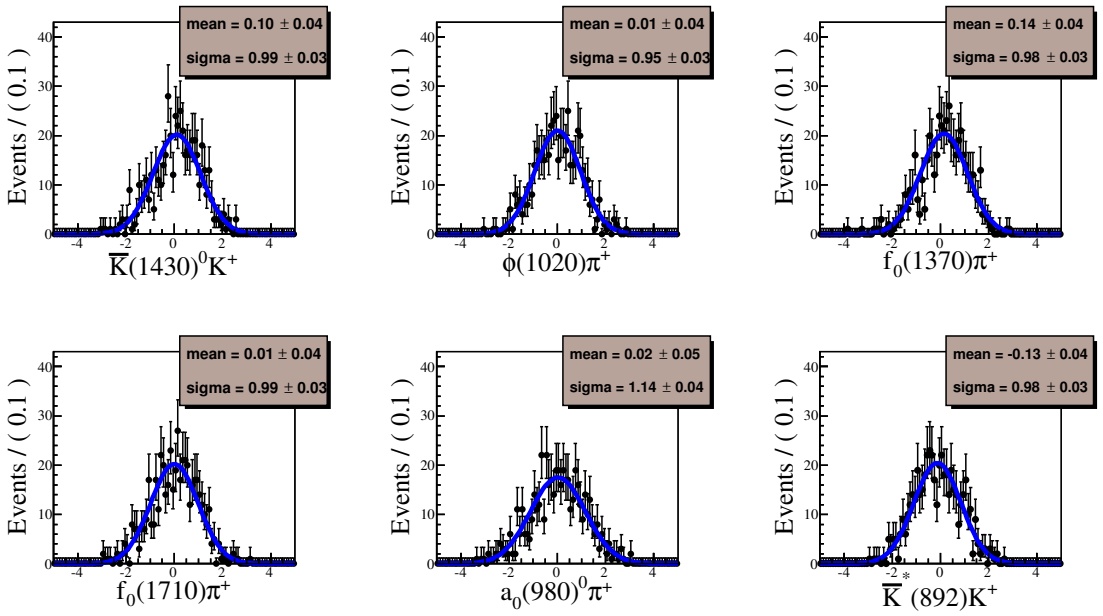


Figure 20: The pull distribution check results for fit fractions of the amplitudes in the nominal fit model.

Table 9: Systematic uncertainties on the $\phi$ and FFs for different amplitudes in units of the corresponding statistical uncertainties.

| Amplitude | | Source | | | | |
|---|---|---|---|---|---|---|
| | | I | II | III | IV | Total |
| $D_s^+ \to \bar{K}^*(892)^0K^+$ | FF | 0.32 | 0.29 | 0.13 | 0.41 | 0.61 |
| $D_s^+ \to \phi(1020)\pi^+$ | $\phi$ | 0.49 | 0.10 | 0.06 | 0.07 | 0.51 |
| | $\rho$ | 0.49 | 0.14 | 0.18 | 0.41 | 0.68 |
| | FF | 0.44 | 1.13 | 0.05 | 0.40 | 1.28 |
| $D_s^+ \to f_0(980)\pi^+/a_0(980)\pi^+$ | $\phi$ | 0.98 | 0.25 | 0.06 | 0.11 | 1.02 |
| | $\rho$ | 1.11 | 0.17 | 0.10 | 0.11 | 1.13 |
| | FF | 1.16 | 0.15 | 0.06 | 0.09 | 1.18 |
| $D_s^+ \to \bar{K}_0^*(1430)^0K^+$ | $\phi$ | 1.02 | 0.48 | 0.09 | 0.21 | 1.15 |
| | $\rho$ | 1.00 | 0.36 | 0.13 | 0.20 | 1.09 |
| | FF | 0.76 | 0.35 | 0.11 | 0.22 | 0.87 |
| $D_s^+ \to f_0(1710)\pi^+$ | $\phi$ | 0.31 | 0.25 | 0.09 | 0.14 | 0.43 |
| | $\rho$ | 1.17 | 1.23 | 0.07 | 0.11 | 1.70 |
| | FF | 0.71 | 1.21 | 0.05 | 0.16 | 1.42 |
| $D_s^+ \to f_0(1370)\pi^+$ | $\phi$ | 2.66 | 0.27 | 0.11 | 0.09 | 2.68 |
| | $\rho$ | 1.01 | 0.32 | 0.06 | 0.09 | 1.06 |
| | FF | 0.42 | 0.30 | 0.15 | 0.06 | 0.54 |

Table 10: The final results of the magnitudes, phases and fit fractions for the six amplitudes. The first and second uncertainties are the statistical and systematic uncertainties, respectively.

| Amplitude | Magnitude | Phase | Fit fractions(%) |
|---|---|---|---|
| $D_s^+ \to \bar{K}^*(892)^0 K^+$ | 1.0(fixed) | 0.0(fixed) | 48.3±0.9±0.5 |
| $D_s^+ \to \phi(1020)\pi^+$ | 1.09±0.02±0.01 | 6.22±0.07±0.04 | 40.5±0.7±0.9 |
| $D_s^+ \to f_0(980)\pi^+/a_0(980)\pi^+$ | 2.88±0.14±0.16 | 4.77±0.07±0.07 | 19.3±1.7±2.0 |
| $D_s^+ \to \bar{K}_0^*(1430)^0 K^+$ | 1.26±0.14±0.15 | 2.91±0.20±0.23 | 3.0±0.6±0.5 |
| $D_s^+ \to f_0(1710)\pi^+$ | 0.79±0.08±0.14 | 1.02±0.12±0.05 | 1.9±0.4±0.6 |
| $D_s^+ \to f_0(1370)\pi^+$ | 0.58±0.08±0.08 | 0.59±0.17±0.46 | 1.2±0.4±0.2 |

# 6 Branching Fraction Measurements

## 6.1 Event Selection

After the selection described in Set.3, we continue to select signals used in this part. We use the same 8 tag modes as in Sec.5.1. In the selection of tag $D_s$, for multiple candidates, the best candidate is chosen with $M_{rec}$ closest to mass of $D_s^*$ in [2]. To further remove the background associated with the larger number of soft $\pi^{\pm}(\pi^0)$ from $D_s^*$ decays, candidates are voted if the momentum of $\pi^{\pm}(\pi^0)$ is less than $0.1GeV$.

The single tag(ST) yields are extracted from the fits to the $D_s$ invariant mass distributions, as shown in Fig.21. In the fit, the mass windows of the tag modes are set to be the same as the Ref. [15]. The signal shape is modeled as MC shape convoluted with a Gaussian function, while background is parameterized as the 2nd-order Chebychev polynomial. The corresponding ST efficiencies are estimated from generic MC. The ST yields($Y_{ST}$) and ST efficiencies($\epsilon_{ST}$) are listed in Table11

Table 11: The ST yields($Y_{ST}$) and ST efficiencies($\epsilon_{ST}$). The mass windows use the results in Ref. [15]

| Tag mode | Mass window(GeV) | $Y_{ST}$ | $\epsilon_{ST}(\%)$ |
|---|---|---|---|
| $D_s^- \to K_S^0 K^-$ | [1.948, 1.991] | 965265 ± 1286 | 49.48±0.07 |
| $D_s^- \to K^+K^-\pi^-$ | [1.900, 2.030] | 4254481 ± 2947 | 42.17±0.03 |
| $D_s^- \to K^+K^-\pi^-\pi^0$ | [1.947, 1.982] | 1161036 ± 3400 | 10.61±0.03 |
| $D_s^- \to K_S^0 K^-\pi^+\pi^-$ | [1.958, 1.980] | 233225 ± 1467 | 19.30±0.12 |
| $D_s^- \to K_S^0 K^+\pi^-\pi^-$ | [1.953, 1.983] | 484801 ± 1312 | 22.72±0.06 |
| $D_s^- \to \pi^-\pi^-\pi^+$ | [1.952, 1.984] | 1152623 ± 3370 | 56.94±0.17 |
| $D_s^- \to \pi^-\eta'_{\pi^+\pi^-\eta_{\gamma\gamma}}$ | [1.940, 1.996] | 251617 ± 737 | 20.43±0.06 |
| $D_s^- \to K^-\pi^+\pi^-$ | [1.953, 1.983] | 610925 ± 2902 | 47.18±0.22 |

After selected the candidates of tag $D_s$, for each tag mode, we can get double tag candidates. We retain the candidates with minimum average mass ($aM$) of tag $D_s$ and signal $D_s$.

With the updated MC sample(DIY MC) based on the amplitude analysis results obtained from the fit to data, the double efficiencies are determined and listed in Table12.

## 6.2 Analytic Strategy

The data sample for this analysis is collected at $E_{cm} = 4.178GeV$, about $100MeV$ higher than $D_s^*D_s$ threshold. Around this energy region, based on the cross section measurement by CLEO [12], we know that most $D_s$ production in $e^+e^-$ collision comes from $D_s^{*\pm}D_s^{\mp}$ events with its cross section approximately $0.9nb$, while the cross section for $D_s^+D_s^-$ is about a factor of 20 smaller. The $D_s^*$ decays to either $\gamma D_s$

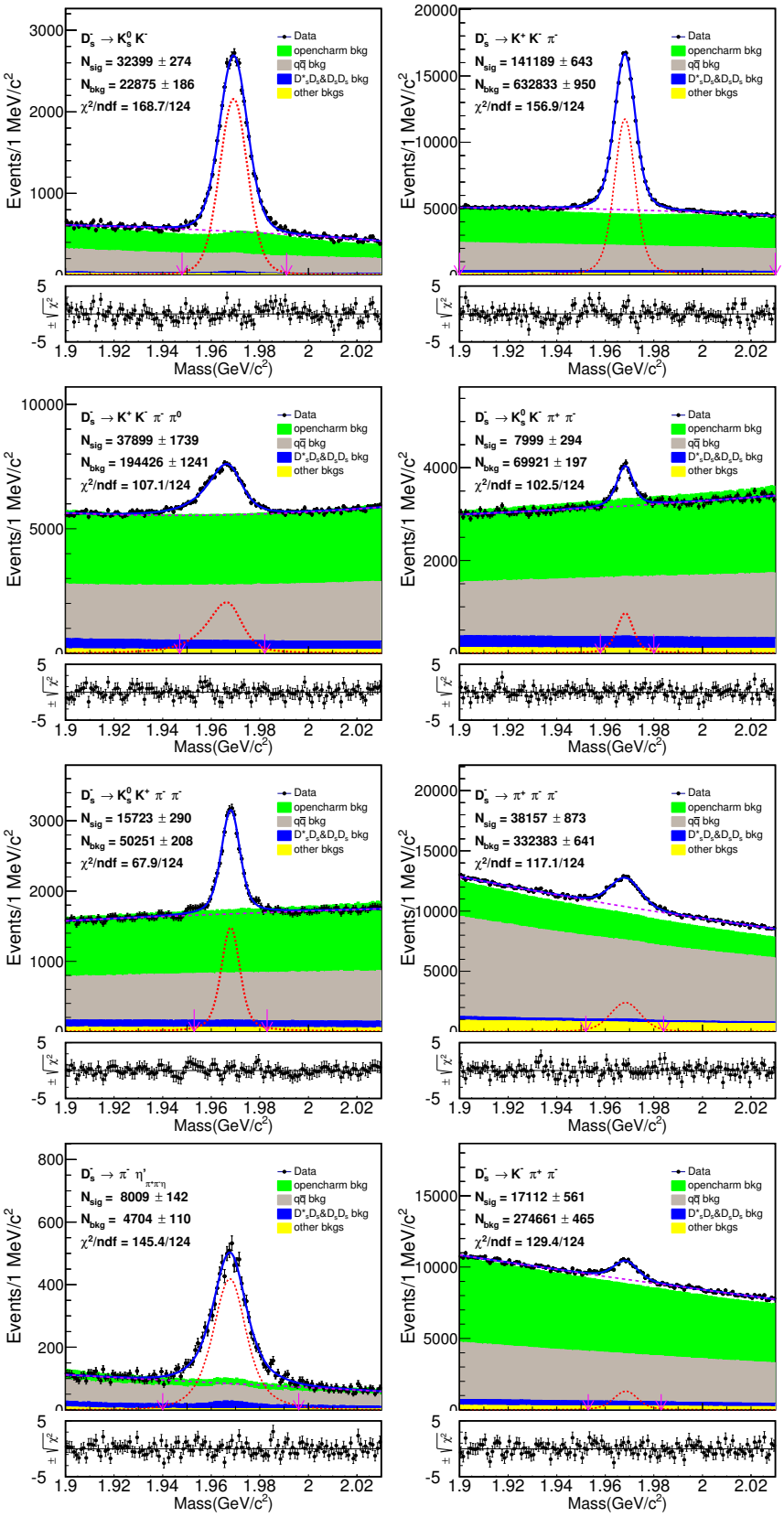


Figure 21: Ds Mass fits from data. The points with error bars are data, and the blue line is the fit. Red short-dashed lines are signal, violet long-dashed lines are background. The red arrows denote the signal region.

Table 12: The DT efficiencies($\epsilon_{DT}$).

| Tag mode | $\epsilon_{DT}(\%)$ |
|---|---|
| $D_s^- \to K_S^0 K^-$ | 19.77±0.14 |
| $D_s^- \to K^+K^-\pi^-$ | 18.21±0.06 |
| $D_s^- \to K^+K^-\pi^-\pi^0$ | 4.69±0.03 |
| $D_s^- \to K_S^0 K^-\pi^+\pi^-$ | 8.34±0.11 |
| $D_s^- \to K_S^0 K^+\pi^-\pi^-$ | 9.55±0.09 |
| $D_s^- \to \pi^-\pi^-\pi^+$ | 23.72±0.15 |
| $D_s^- \to \pi^-\eta'_{\pi^+pi^-\eta_{\gamma\gamma}}$ | 8.70±0.11 |
| $D_s^- \to K^-\pi^+\pi^-$ | 19.68±0.17 |

or $\pi^0 D_s$ with branching fractions of $(93.5 \pm 0.7)\%$ and $(5.8 \pm 0.7)\%$ [2], respectively. The other charm productions total $7pb$ mainly including $D^*\bar{D}^*$ with a cross section of $5nb$, $D^*\bar{D} + D\bar{D}^*$ with a cross section of $2nb$, and $D\bar{D}$ with a cross section of relatively small $0.2nb$. There also appears to be $D\bar{D}^*\pi$ production. The underlying light quark "continuum" background is about $12nb$. The relatively large cross sections, relatively large branching fractions, and sufficient luminosities allow us to employ double tag (DT) technique to study this study.

As $D_s^- \to K^+K^-\pi^-$ is not only our signal mode but also one of our tag modes, we divide the events into two categories:

- Cat. A: Tag $D_s$ decays to tag modes except $D_s^- \to K^+K^-\pi^-$. The generic MC sample with the signal removed shows no peaking background around the fit range of $1.90 < M_{sig} < 2.03GeV$. Thus, the double tag yield is determined by the fit to $M_{sig}$, which has shown in Fig.22(a).And the background is described with $2^{nd}$-order Chebychev polynomial. The double tag yield is $3484 \pm 64$.

- Cat. B: Tag $D_s$ decays $K^+K^-\pi^+$. As both of the two $D_s$ mesons decay to our signal modes, we fit $aM$(the average mass of $D_s$ at signal side and tag side), which is shown in Fig.22(b). Here, the background is described with $2^{nd}$-order Chebychev polynomial. The double tag yield is $1651 \pm 42$.

To measure the branching fraction of this decay, we start from the following equations with one tag mode:

$$N_{tag}^{obs} = 2N_{D_s^+D_s^-}\mathcal{B}_{tag}\epsilon_{tag}, \tag{27}$$

$$\begin{aligned} N_{sig}^{obsA} &= 2N_{D_s^+D_s^-}\mathcal{B}_{tag}\mathcal{B}_{sig}\epsilon_{tag,sig}, \quad \text{for Cat. A} \\ N_{sig}^{obsB} &= N_{D_s^+D_s^-}\mathcal{B}_{tag}\mathcal{B}_{sig}\epsilon_{tag,sig}, \quad \text{for Cat. B} \end{aligned} \tag{28}$$

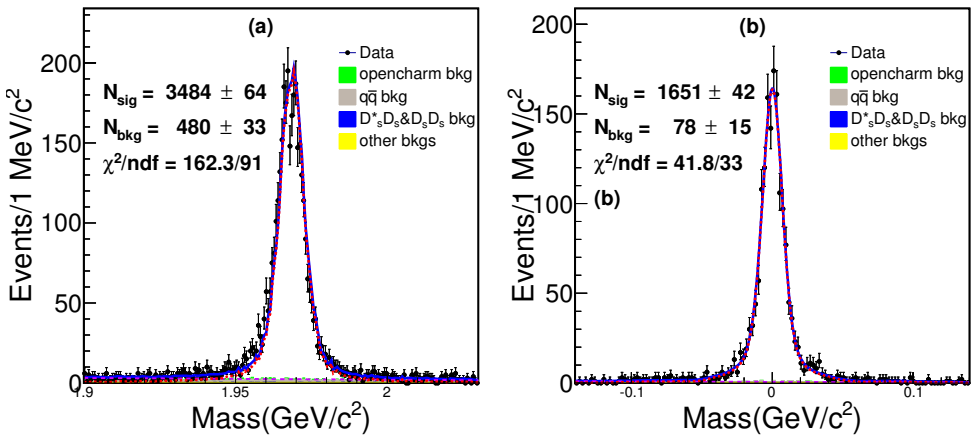


Figure 22: Fit of (a)Cat. A and (b)Cat. B. We fit $M_{sig}$ and $aM$ for Cat. A and Cat. B, respectively. The signal shapes are the corresponding simulated shapes convoluted with a Gaussian function and the background shapes are described with $2^{nd}$-order Chebychev polynomial.

where $N_{D_s^+D_s^-}$ is the total number of $D_s^{*\pm}D_s^{\mp}$ produced from $e^+e^-$ collision; $N_{tag}^{obs}$ is the number of observed tag modes; $N_{sig}^{obsA}$ and $N_{sig}^{obsB}$ are the number of observed signals for Cat. A and Cat. B, respectively; $\mathcal{B}_{tag}$ and $\mathcal{B}_{sig}$ are the branching fractions of specific tag mode and signal mode, respectively; $\epsilon_{tag}$ is the reconstruction efficiency of the tag mode; $\epsilon_{tag,sig}$ is the reconstruction efficiency of both the tag and signal decay modes.

Using the above equations, it's easy to obtain:

$$\mathcal{B}_{sig} = \frac{N_{sig}^{obsA} + 2N_{sig}^{obsB}}{\sum_\alpha N_{tag}^\alpha \epsilon_{tag,sig}^\alpha / \epsilon_{tag}^\alpha}, \tag{29}$$

where the yields $N_{tag}^{obsA}$, $N_{tag}^{obsB}$ and $N_{tag}^{\alpha}$ can be obtained from data, while $\epsilon_{tag}$ and $\epsilon_{tag,sig}$ can be obtained from the appropriate MC samples, $\alpha = 1, 2, 3...$ represents the tag mode.

## 6.3 Results of Branching Fraction

Then we can get the branching fraction $\mathcal{B}(D_s^+ \to K^+K^-\pi^+) = (5.47 \pm 0.07)\%$(only statistical uncertainty) according to Eq.29.

## 6.4 Systematic Uncertainties

The following sources are taken in account to calculate systematic uncertainties.

- Signal shape. The systematic uncertainty due to the signal shape is studied with the fit without the Gaussian function convoluted, the double tag yield shift is taken as the related effect.

- Background shape and fit range. For background shape and the fit range, the MC shape is used to instead the $1^{st}$-order Chebychev polynomial and the fit range of $[1.90, 2.03]GeV$ is changed to $[1.89, 2.04]GeV$. The largest branching fraction shift is taken as the related effect.

- Fit bias. The possible bias is estimated by the IO check using the round 30-40 of generic MC, which is shown in Table 13. The estimated mean ($\mu_{\mathcal{B}}$) and its uncertainty ($\sigma_{\mu}$) is calculated with the following formulas:

$$\mu_{\mathcal{B}} = \frac{\sum_i \frac{\mu_i}{\sigma_i^2}}{\sum_i \frac{1}{\sigma_i^2}}, \quad \sigma_{\mu}^2 = \sum_i \frac{1}{\sigma_i^2}, \tag{30}$$

  where $\mu_i$ and $\sigma_i$ are the measured branching fraction value and its statistical uncertainty for the sample i. The combined result of the round 30-40 is $\mu_{\mathcal{B}} = (5.462 \pm 0.021)\%$. The relative change compared to the input value is 0.1%.

Table 13: IO check using the round 30-40 of generic MC.

| Round | $\mathcal{B}(D_s^+ \to K^+K^-\pi^+)(\%)$ |
|---|---|
| 31 | $5.562 \pm 0.066$ |
| 32 | $5.497 \pm 0.066$ |
| 33 | $5.407 \pm 0.066$ |
| 34 | $5.636 \pm 0.068$ |
| 35 | $5.490 \pm 0.066$ |
| 36 | $5.397 \pm 0.066$ |
| 37 | $5.369 \pm 0.066$ |
| 38 | $5.490 \pm 0.067$ |
| 39 | $5.353 \pm 0.065$ |
| 40 | $5.435 \pm 0.066$ |
| Combined result | $5.462 \pm 0.021$ |

- $K^{\pm}$ and $\pi^{\pm}$ Tracking/PID efficiency. Based on the works [21] and [22] by Xingyu Shan and Sanqiang Qu, etc. we find that it's enough to assign 1.1% , 0.4%, 1.1% and 0.2% as the systematic uncertainty for $K^{\pm}$ PID, $\pi^{\pm}$ PID, $K^{\pm}$ tracking, $\pi^{\pm}$ tracking efficiencies, respectively.

- MC statistics. The uncertainty of MC statistics is obtained by $\sqrt{\sum_i f_i \frac{\delta_{\epsilon_i}}{\epsilon_i} i}$, where $f_i$ is the tag yield fraction and $\epsilon_i$ is the signal efficiency of tag mode $i$.

All of the systematic uncertainties mentioned above are summarized in Table 14.

The branching fraction with systematic uncertainties is $\mathcal{B}(D_s^+ \to K^+K^-\pi^+) = (5.47 \pm 0.07_{stat.} \pm 0.13_{sys.})\%$.

Table 14: Systematic uncertainties of branching fraction.

| Source | Sys. Uncertainty |
|---|---|
| Signal shale | 0.3 |
| Background shape and fit range | 1.1 |
| Fit bias | 0.1 |
| $K^{\pm}$ and $\pi^{\pm}$ PID efficiency | 1.5 |
| $K^{\pm}$ and $\pi^{\pm}$ Tracking efficiency | 1.3 |
| MC statistics | 0.2 |
| total | 2.3 |

# 7 Summary

This analysis presents the amplitude analysis for the decay $D_s^+ \to K^+K^-\pi^+$. Table 15 is a comparison of amplitude analysis between BABAR, CLEO-c and this analysis. Our results are roughly consistent with those of BABAR and CLEO-c. And for the fit fraction of $D_s^+ \to f_0(980)\pi^+/a_0(980)\pi^+$, we tend to agree the result of BABAR.

Table 15: Comparision of fit fraction between BABAR, CLEO-c and this amplitude analysis.

| Amplitude | BABAR | CLEO-c | This Analysis |
|---|---|---|---|
| $D_s^+ \to \bar{K}^*(892)^0K^+$ | 47.9±0.5±0.5 | 47.4±1.5±0.4 | 48.3±0.9±0.5 |
| $D_s^+ \to \phi(1020)\pi^+$ | 41.4±0.8±0.5 | 42.2±1.6±0.3 | 40.5±0.7±0.9 |
| $D_s^+ \to f_0(980)\pi^+/a_0(980)\pi^+$ | 16.4±0.7±2.0 | 28.2±1.9±1.8 | 19.3±1.7±2.0 |
| $D_s^+ \to \bar{K}_0^*(1430)^0K^+$ | 2.4±0.3±1.0 | 3.9±0.5±0.5 | 3.0±0.6±0.5 |
| $D_s^+ \to f_0(1710)\pi^+$ | 1.1±0.1±0.1 | 3.4±0.5±0.3 | 1.9±0.4±0.6 |
| $D_s^+ \to f_0(1370)\pi^+$ | 1.1±0.1±0.2 | 4.3±0.6±0.5 | 1.2±0.4±0.2 |
| $\sum FF(\%)$ | 110.2±0.6±2.0 | 129.5±4.4±2.0 | 114.2±1.7±2.3 |
| $\chi^2/NDF$ | $\frac{2843}{2305-14} = 1.2$ | $\frac{178}{117} = 1.5$ | $\frac{290}{291-10-1} = 1.04$ |
| Events | 96307 ± 369(purity 95%) | 14400(purity 85%) | 4381(purity 99.7%) |

In this analysis, as $a_0(980)$ and $f_0(980)$ are close to each other and parameters of $f_0(980)$ is not well measured, we have to take $f_0(980)$ and $a_0(980)$ as a whole, that is the $\mathcal{S}$ wave at the low end of $K^+K^-$ mass spectrum. The $\mathcal{S}$ wave is extracted with the model independent method.

We also measure the branching fraction and the value is $\mathcal{B}(D_s^+ \to K^+K^-\pi^+) = (5.47 \pm 0.07_{stat.} \pm 0.13_{sys.})\%$. As is shown in Table 16, the branching fraction of this analysis has the best precision.

Table 16: Comparisons of branching fraction between BABAR, CLEO-c and this analysis.

| $\mathcal{B}\,(D_s^+ \to K^+K^-\pi^+)(\%)$ | Collaboration |
|---|---|
| $5.55 \pm 0.14_{stat.} \pm 0.13_{sys.}$ | CLEO-c [23] |
| $5.06 \pm 0.15_{stat.} \pm 0.21_{sys.}$ | BELLE [24] |
| $5.78 \pm 0.20_{stat.} \pm 0.30_{sys.}$ | BABAR [25] |
| $5.47 \pm 0.07_{stat.} \pm 0.13_{sys.}$ | BESIII(this analysis) |

# References


[1] Yu Lu and Liaoyuan Dong, BESIII DocDB 682-v7.

[2] K. A. Olive *et al.* (Particle Data Group), Chin. Phys. C **40**, 100001 (2016)

[3] B. Aubert *et al.* (BABAR Collaboration), Phys. Rev. D**74**, 032003 (2006).

[4] M. Ablikim *et al.* (BES2 Collaboration), Phys. Rev. D**72**, 092002 (2005).

[5] V.V. Anisovich *et al.*, PAN **65** 1545 (2002).

[6] H. Y. Cheng, Phys. Rev. D**67**, 094007 (2003).

[7] H. Y. Cheng and C. W. Chiang, Phys. Rev. D**81**, 074031 (2010).

[8] H. Y. Cheng, Phys. Lett. B**707**, 116 (2012).

[9] P.L. Frabetti *et al.* (E687 Collaboration), Phys. Lett. B**351**, 591 (1995).

[10] R.E. Mitchell *et al.* (CLEO Collaboration), Phys. Rev. D**79**, 072008 (2009).

[11] P.del Amo Sanchez *et al.* (BARBAR Collaboration), Phys. Rev. D**83**, 052001 (2011).

[12] D.Cronin-Hennessy *et al.* (CLEO Collaboration), Phys. Rev. D**80**, 072001 (2009).

[13] Andy Julin, Hajime Muramatsu and Ron Poling, BESIII DocDB 580-v1.

[14] C. Patrignani *et al.* (Paritcle Data Group), Chin. Phys. C 40,100001 (2016)

[15] Sifan Zhang and Hailong Ma, BESIII DocDB 630-v35.

[16] Yu Lu and Liaoyuan Dong, BESIII DocDB 416-v30.

[17] B. S. Zou and D. V. Bugg, Eur. Phys. J. A**16**, 537(2003).

[18] M. Alblikim *et al.* (BESIII Collaboration), Phys. Lett. B**607** 243 (2005).

[19] G. Bonvicini *et al.* (CLEO Collaboration), Phys. Rev. D**78**, 052001 (2001).

[20] Yu Lu and Liaoyuan Dong, BESIII DocDB 613-v16.

[21] https://indico.ihep.ac.cn/event/8006/contribution/1/material/slides/0.pdf

[22] https://indico.ihep.ac.cn/event/8023/contribution/1/material/slides/0.pdf

[23] P.U.E. Onyisi *et al.* (CLEO Collaboration), Phys. Rev. D**88**, 032009 (2013).

[24] A. Zupanc *et al.* (BELLE Collaboration), JHEP **1309**, 139 (2013).

[25] P. del Amo Sanchez *et al.* (BABAR Collaboration), Phys. Rev. D**82**, 091003 (2010).